Characterising the Far-infrared Properties of Distant X-ray Detected AGNs: Evidence for Evolution in the Infrared–X-ray Luminosity Ratio

J. R. Mullaney[1]⋆, D. M. Alexander[1], M. Huynh[2], A. D. Goulding[1] & D. Frayer[2]

[1]*Department of Physics and Astronomy, Durham University, South Road, Durham, DH1 3LE, U.K.*
[2]*Infrared Processing and Analysis Center, California Institute of Technology, 100-22, Pasadena, CA 91125*

ABSTRACT

We investigate the far-infrared properties of X-ray sources detected in the *Chandra* Deep Field-South (CDF-S) survey using the ultra-deep 70 μm and 24 μm *Spitzer* observations taken in this field. Since only 30 (i.e., $\approx 10\%$) of the 266 X-ray sources in the region of the 70 μm observations are detected at 70 μm, we rely on stacking analyses of the 70 μm data to characterise the average 70 μm properties of the X-ray sources as a function of redshift, X-ray luminosity and X-ray absorption. Using *Spitzer*-IRS data of the *Swift*-BAT sample of $z \approx 0$ active galactic nuclei (hereafter, AGNs), we show that the 70/24 μm flux ratio can distinguish between AGN-dominated and starburst-dominated systems out to $z \approx 1.5$. Among the X-ray sources detected at 70 μm we note a large scatter in the observed 70/24 μm flux ratios, spanning almost a factor of 10 at similar redshifts, irrespective of object classification, suggesting a range of AGN:starburst ratios. From stacking analyses we find that the average observed 70/24 μm flux ratios of AGNs out to an average redshift of 1.5 are similar to $z \approx 0$ AGNs with similar X-ray luminosities ($L_X = 10^{42-44}$ erg s^{-1}) and absorbing column densities ($N_H \leqslant 10^{23}$ cm^{-2}). Furthermore, both high redshift and $z \approx 0$ AGNs follow the same tendency toward warmer 70/24 μm colours with increasing X-ray luminosity (L_X). From analyses of the *Swift*-BAT sample of $z \approx 0$ AGNs, we note that the 70 μm flux can be used to determine the infrared (8-1000 μm) luminosities of high redshift AGNs. We use this information to show that $L_X = 10^{42-43}$ erg s^{-1} AGNs at high redshifts ($z = 1-2$) have infrared to X-ray luminosity ratios (hereafter, L_{IR}/L_X) that are, on average, $4.7^{+10.2}_{-2.0}$ and $12.7^{+7.1}_{-2.6}$ times higher than AGNs with similar X-ray luminosities at $z = 0.5-1$ and $z \approx 0$, respectively. By comparison, we find that the L_{IR}/L_X ratios of $L_X = 10^{43-44}$ erg s^{-1} AGNs remain largely unchanged across this same redshift interval. We explore the consequences that these results may have on the identification of distant, potentially Compton-thick AGNs using L_{IR}/L_X ratios. In addition, we discuss possible scenarios to account for the observed increase in the L_{IR}/L_X ratio with redshift, including changes in the dust covering factor of AGNs and/or the star formation rates of their host galaxies. Finally, we show how deep observations to be undertaken by the *Herschel Space Observatory* will enable us to discriminate between these proposed scenarios and also identify Compton-thick AGNs at high redshifts.

Key words: galaxies: Active Galaxies, High Redshift, Infrared: Galaxies, X-rays: Galaxies

1 INTRODUCTION

Deep X-ray surveys undertaken by the *Chandra* and *XMM-Newton* observatories have provided the most efficient method to date of identifying large numbers of active galactic nuclei (hereafter, AGNs) out to high redshifts ($z \approx 5$; e.g., Alexander et al. 2001; Barger et al. 2003; Bauer et al. 2004; Szokoly et al. 2004;

Brandt & Hasinger 2005; Mainieri et al. 2005). Due to the high penetrating power of hard (i.e., >2 keV) X-rays, they provide a means of identifying AGNs that is much less biased toward unobscured AGNs than, for example, that obtained at optical wavelengths alone. Consequently, deep X-ray surveys have revealed that a large fraction (up to $\approx 75\%$; Mainieri et al. 2002; Dwelly & Page 2006; Tozzi et al. 2006; Tajer et al. 2007) of highly obscured AGNs are often unidentified or misclassified by observations at other wavelengths (e.g. Barger et al. 2003; Szokoly et al. 2004). Further-

⋆ E-mail: j.r.mullaney@dur.ac.uk

more, as the central engines of AGNs are the only compact objects capable of producing luminous X-ray emission (i.e., $L_X > 10^{42}$ erg s^{-1}), observations at these high energies provide the most reliable method of measuring the intrinsic power of the central engine without suffering from significant contamination by star-formation.

Although X-rays provide an ideal means of studying the central engines of AGNs, they yield limited information on the regions outside the central few parsecs. For example, although X-ray observations have been used extensively to measure the amount of absorbing gas (i.e. N_H) *along our line of sight* to the central engine (e.g. Mushotzky et al. 1993; Bassani et al. 1999; Malizia et al. 2003; Guainazzi et al. 2005), they tell us little about the spatial extent and covering factor of the putative obscuring dusty torus, a key component of the unification models that have become a cornerstone of AGN research over the past two decades (e.g. Antonucci & Miller 1985; Krolik & Begelman 1988; Antonucci 1993). Furthermore, as any X-ray emission from stellar processes will be swamped by the presence of an AGN, X-rays alone provide little insight into the relationship between star-formation and AGN activity that is predicted by both galaxy formation models (e.g. Kauffmann & Haehnelt 2000; Benson et al. 2003; Granato et al. 2004; Bower et al. 2006; Booth & Schaye 2009) and locally defined black hole–bulge relationships (e.g. Magorrian et al. 1998; Gebhardt et al. 2000; Tremaine et al. 2002; McLure & Dunlop 2002). Observations at infrared (hereafter, IR) wavelengths can provide significant insights on both these counts.

Like X-rays, the longer IR wavelengths (i.e., >5 μm) are largely unaffected by absorption from interstellar gas/dust. However, because IR radiation is typically produced via the reprocessing of shorter wavelength light by dust, it also provides a means to study the dusty environments surrounding AGNs. Furthermore, as both AGNs and starbursting systems are capable of producing large amounts of IR radiation, the study of AGNs at these wavelengths can provide insights into the processes that connects AGN activity and star-formation. However, despite considerable gains in our understanding of the IR properties of AGNs since the launch of the *Spitzer Space Telescope*, there remains many unresolved questions. For example, we currently lack a clear picture of how the IR emission of AGNs is affected by the differences in the intrinsic power of the central engine and, perhaps more importantly, whether it evolves over cosmic time. As a result, our understanding of both the putative torus and the interplay between AGN activity and star-formation is limited.

To date, most studies of the IR properties of AGNs have concentrated on the relatively short wavelength data provided by the IRAC instrument (3.6 μm, 4.5 μm, 5.8 μm and 8.0 μm) and the 24 μm observations taken with the MIPS instrument on-board the *Spitzer Space Telescope* (e.g. Lutz et al. 2004; Stern et al. 2005; Donley et al. 2007; Daddi et al. 2007). However, studies of high redshift objects at these shorter wavelengths are hindered by the presence of strong spectral features at $\lambda\lambda \lesssim 12$ μm (in particular polycyclic aromatic hydrocarbons [PAHs], silicate absorption features and strong emission lines) that shift into these wavebands at $z \gtrsim 0.7$. For example, the IR luminosities of high redshift galaxies are overestimated by a factor of $\sim 2-5$ (depending on redshift and L_{IR}) when using 24 μm data alone compared to that calculated using the full IR SED incorporating longer wavelength data (at 70 μm and 160 μm; see Papovich et al. 2007; Magnelli et al. 2009, Magnelli et al. 2009 [in prep.]). Furthermore, as emission from high redshift starbursting systems peaks at longer wavelengths than those probed by the 24 μm waveband, the sole use of near and mid-

IR observations hampers our ability to efficiently distinguish between star-formation and AGN dominated systems. This too can be resolved by incorporating longer wavelength IR data into our analysis. Undoubtedly, the launch of the *Herschel Space Telescope*, with its ability to observe the universe at $55 - 672$ μm, will help in addressing these issues. However, progress can be made now by applying stacking analyses to deep *Spitzer* 24 μm and 70 μmobservations, enabling us to measure the average IR properties of AGNs at a sensitivity level comparable to that achievable for individual sources in the proposed deep *Herschel* fields (e.g. the HGOODS Key Programme[1]; PI: D. Elbaz).

In this paper we investigate the mid to far-IR properties of X-ray detected AGNs that lie in the confusion-limited 70 μm and 24 μm *Spitzer*-MIPS Far-Infrared Deep Extragalactic Legacy Survey (FIDEL) and Great Observatories Origins Deep Survey (GOODS). We identify AGNs using the 1 Ms *Chandra* Deep Field-South X-ray observations (which have high quality X-ray spectral constraints published in Tozzi et al. 2006) and explore their 70 μm fluxes, luminosities, and 70/24 μm flux ratios (hereafter, S_{70}/S_{24}) as a function of redshift, X-ray luminosity, and X-ray absorption. As part of our analysis we use the *Swift*-BAT sample of local, well studied AGNs to develop diagnostics to distinguish between starburst (hereafter, SB) and AGN dominated systems at $z \lesssim 1.5$. In the CDF-S field we find evidence that more X-ray luminous AGNs have warmer, more AGN dominated IR colours and that high–z, low X-ray luminosity (i.e., $z = 1-2$, $L_X = 10^{42-43}$ erg s^{-1}) AGNs are significantly more IR luminous than their low redshift counterparts (i.e., $z = 0.5-1$, $L_X = 10^{42-43}$ erg s^{-1}). This increase in IR luminosity may be interpreted as tentative evidence of larger dust covering factors in high redshift AGNs, supporting results from deep X-ray surveys which find evidence of larger levels of N_H at similar redshifts (e.g. La Franca et al. 2005; Hasinger 2008. However, a proportion of this increase may also be attributed to higher levels of star-formation in these systems. We show that deep, far-IR *Herschel* surveys will resolve the dominant process behind this increase in IR luminosity and enable the discrimination between AGN and star-formation dominated systems out to $z \approx 5-6$.

Throughout this work we adopt $H_0 = 71$ km s^{-1} Mpc^{-1}, $\Omega_M = 0.27$, and $\Omega_\Lambda = 0.73$. We report 1σ errors for detected sources and provide 3σ upper limits for undetected sources ($<3σ$).

2   DATA

Our main focus throughout this work is the analysis of the mid and far-infrared (MIR [5–30 μm] and FIR [30–300 μm], respectively) emission of X-ray detected sources in the CDF-S field. To aid in the interpretation of the CDF-S data, we also make use of archival *Spitzer*-IRS spectra and *IRAS* data for the *Swift*-BAT sample of local X-ray AGNs, two archetypal AGNs (NGC 1068 and NGC 6240), and a distant quasi-stellar object (QSO) sample. We describe the CDF-S sample in §2.1 and the comparison samples in §2.2.

2.1   CDF-S Sample of X-ray Detected AGNs & Starbursts

2.1.1   *Chandra Data*

The X-ray data for our main sample are taken from the 1 Ms CDF-S X-ray observations (Giacconi et al. 2002), as analysed by

---

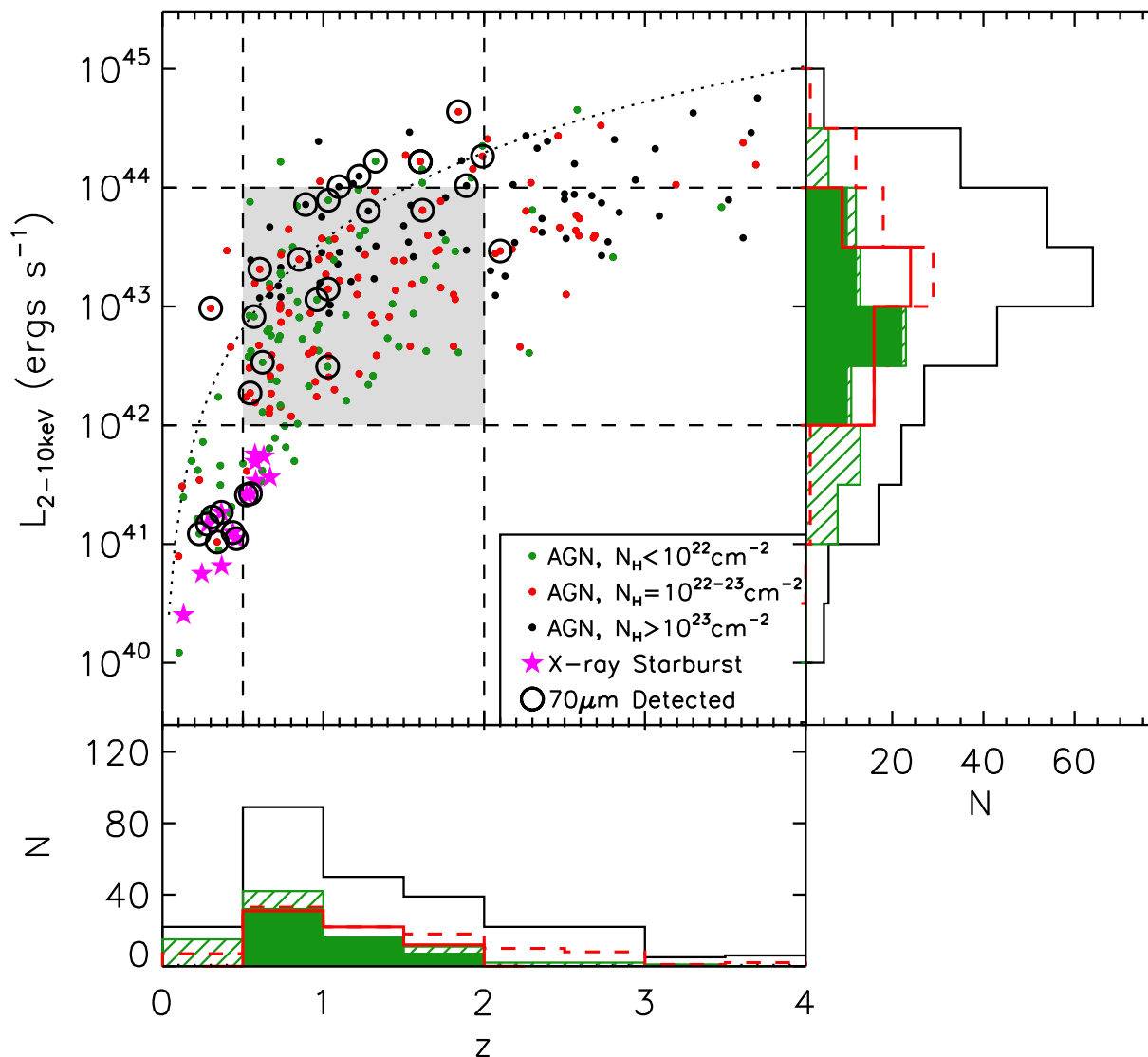[1] URL: http://herschel.esac.esa.int/Docs/KPOT/GOODS_Herschel.pdf

Figure 1. Rest-frame hard X-ray luminosity ($L_{2\text{-}10\text{keV}}$) vs. redshift ($z$) of the AGNs and SBs identified in the 1 Ms CDF-S X-ray observations, separated according to column density (N_H). Those sources detected at 70 μm are indicated with large circles. As described in §2.1.1 this sample contains biases in favour of more luminous sources and higher column densities at higher redshifts. To mitigate the effects of these biases we define a more heterogeneous subsample (the 'Restricted' sample), contained within the grey shaded region. Coloured histograms indicate the number of AGNs in each redshift and X-ray luminosity bin that have column densities $N_H < 10^{22}$ cm^{-2} (green) and $N_H = 10^{22-23}$ cm^{-2} (red). The black histogram shows the distribution of the full AGN+SB sample. Solid colours/lines are used to indicate the restricted sample, hatching/dashes indicate the (unrestricted, flux limited) parent sample. The curved dotted line indicates the constant, unabsorbed hard X-ray flux (6.8×10^{-15} erg s^{-1} cm^{-2}) that best fits the L_X-z distribution of the 70 μm detected X-ray AGNs.

Alexander et al. (2003). In total there are 201, 304, and 326 X-ray detected objects in this region down to limiting 2-8 keV fluxes of 10^{-15}, 10^{-16} and 10^{-17} erg s^{-1} cm^{-2}, respectively. The CDF-S data is deep enough to detect star-formation activity out to $z \approx 1$. Since the primary aim of this study is to explore the IR properties of X-ray detected AGNs, we have used the Bauer et al. (2004) X-ray source classifications to separate AGNs from star-forming galaxies. In the full catalogue of X-ray sources, there are 288 X-ray AGNs and 15 X-ray SBs (the remaining 23 are classed as either normal galaxies or stars and are excluded from further discussion). The absorption corrected 2–10 keV X-ray luminosities (L_X) and X-ray absorption column densities (N_H) are taken from Tozzi et al. (2006). Here, we only consider those 266 X-ray AGNs/SBs with well defined L_X and N_H measurements. Spectroscopic and photo-

metric redshifts for these 266 X-ray AGNs/SBs were also taken from Tozzi et al. (2006); 137 have spectroscopic redshifts (113 of which are described as secure, see Tozzi et al. 2006 for details). We use photometric redshifts for the remaining 129 X-ray AGNs/SBs that lack spectroscopic redshifts.

In Fig. 1 we present the L_X-redshift distribution of the 266 X-ray AGNs/SBs considered in this study. As is to be expected in flux limited samples, there is a strong bias toward the detection of more luminous sources at higher redshifts. Furthermore, as is shown in Fig. 2, there is a bias toward higher column densities at higher X-ray luminosities because a) only the brightest X-ray sources can be detected behind $N_H > 10^{22-23}$ cm^{-2} and b) it is difficult to measure low values of N_H at high redshifts due to the absorption cut-off being shifted out of the lowest *Chandra* energy band. In our analysis
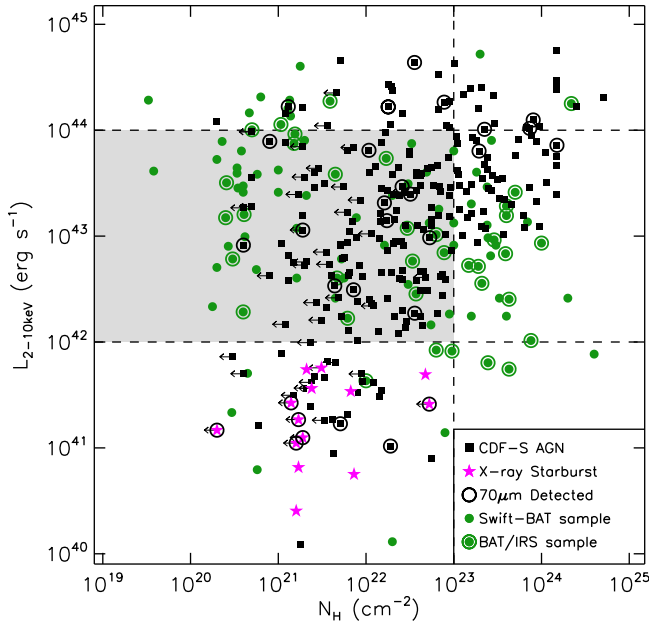
Figure 2. Rest frame hard X-ray luminosity ($L_{2\text{-}10\text{keV}}$) versus column density (N_H) of AGNs and SBs identified in the 1 Ms CDF-S X-ray observations. Also shown is the L_X-N_H distribution of the *Swift*-BAT sample of $z \approx 0$ AGNs which cover the same region of the parameter space as the CDF-S sample. The selection criteria for inclusion in the 'Restricted' sample is indicated by the shaded region.

we consider two main samples: a) the full sample of classified X-ray AGNs/SBs and b) a 'Restricted' sample limited to those AGNs with $L_X = 10^{42-44}$ erg s^{-1} and $N_H < 10^{23}$ cm^{-2} within the redshift range of $0.5 < z < 2.0$ (indicated by the shaded regions in Figs.1 and 2). The 'Restricted' sample is used to mitigate the effects of absorption and selection biases on the average results; the L_X and N_H range of the restricted sample is also well matched to the $z \approx 0$ *Swift*-BAT comparison sample (see §2.2.1).

2.1.2   Spitzer Data

The 24 μm and 70 μm *Spitzer*-MIPS GOODS/CDF-S[2] observations (PID: 20147; P.I.: D. Frayer) and FIDEL[3] legacy surveys (PID: 30948; P.I.: M. Dickinson) are the deepest available at these wavelengths and therefore present the best datasets to study the MIR to FIR emission of AGNs in the high–*z* universe. While the FIDEL region covers the full E-CDFS (Lehmer et al. 2005), the deepest region is the $10' \times 10'$ region centred on the CDF-S field covered by the GOODS observations. The raw 70 μm data were processed off-line using the Germanium Reprocessing Tools (GeRT), following the techniques described in Frayer et al. (2006). The final mosaics, produced by MOPEX[4], have a pixel scale of 4.0″. The 70 μm 3σ sensitivity is 2.0 mJy in the CDF-S field and ≈3.0 mJy in the outer E-CDFS regions. The 24 μm images produced using MOPEX have a pixel scale of 1.2″. The sky coverage at 24 μm is inhomogeneous and the sensitivity ranges from 30 to 70 μJy (5σ). Assuming a SNR of 4.1 for the the 24 μm observations (corre-

sponding to an mean flux limit of ≈50 μJy) there are 14025 detected sources in the FIDEL field.

2.1.3   X-ray–IR source matching

We matched the classified X-ray sources to the 70 μm sources assuming a search radius of 2.0″ for those sources in the GOODS field with 24 μm/IRAC counterparts and 4.0″ in the larger FIDEL field. This yields 30 matches which are listed in Table 1, representing ≈ 11% of the 266 X-ray AGNs/SBs. Using the *P*-statistic ($P = 1 - \exp(-\pi n \theta^2)$; e.g., see Downes et al. 1986 and Eqn 1 in Pope et al. 2006) and a 70 μm source density $n \approx 2.0 \times 10^3$ deg^{-2}, the chance of one or more 70 μm source lying within 4.0″ of an X-ray source is $P \approx 0.2\%$. Given the small value of *P*, it was not necessary to apply the correction to the matching procedure described by Downes et al. (1986).

We matched the X-ray sources to the 24 μm sources using a 3.0″ search radius; this search radius was found to provide the best compromise between finding real matches while reducing the number of spurious matches. Out of the 266 CDF-S X-ray AGN/SBs we found 172 have 24 μm counterparts (i.e., ≈ 65%). The number of spurious matches in the CDF-S field was estimated to be ∼ 4.5% using two approaches (1) by calculating the area of the field covered by 24 μm sources, assuming that each source is a circle of radius 3.0″, and (2) by shifting the positions of the 24 μm sources by a random displacement between 20″ and 55″ and then re-matching to the X-ray sample. This spurious matching fraction is consistent with the *P*-statistic (≈3%), assuming $n \approx 1.5 \times 10^4$ deg^{-2} (see above). In spite of the larger *P*-statistic associated with the 24 μm matches compared to the 70 μm matches, the correction described in Downes et al. (1986) need only be applied to 15 (6%) of the 266 X-ray sources and has negligible effect on any of our results.

All but one of the 70 μm detected sources has a 24 μm counterpart. Further investigation reveals that the lack of a matched 24 μm counterpart is the result of the larger PSF of the 70 μm image; at the corresponding position in the 24 μm image there is a cluster of sources that lie just outside the 3.0″ matching radius which blend to form a single "source" in the 70 μm image. To mitigate source blending we de-blend the 70 μm sources with Gaussians placed at the 24 μm positions. It is these 'de-blended' fluxes that are reported in Table 1.

Finally, one of the 70 μm detected X-ray sources lies within 3.0″ of two 24 μm sources (Tozzi et al. 2006 Index: 31); in Table 1 we list both 24 μm matches but assume that the brighter of the two 24 μm sources is the real match in our analysis.

2.1.4   24 μm and 70 μm stacking procedure

As the majority of the X-ray sources are not detected at 70 μm we rely on stacking analyses to provide insight into their average MIR to FIR properties. Stacking was performed using the code of Huynh et al. (2007). Cutouts of 128″ x 128″ (32 x 32 pixels) were made from the 70 μm image at the stack positions and combined using a weighted mean. The 70 μm stacked flux density was measured using an aperture of 8.0″ at the stacked image center. Offset stacks were generated using random but nearby offset positions (< 64″) in the 70 μm image. Two hundred randomly offset stacks were made and the uncertainty in the stacked flux is taken as the standard deviation of the measured flux density in the 200 offset stacks.

We created stacks that either include or exclude the 70 μm

---

detected sources; the former (hereafter, *"all"*) provides a global average of the FIR properties of all X-ray sources and the latter (hereafter, *"undetected"*) provides the average of the 70 μm undetected X-ray sources that is less skewed by individual bright 70 μm sources. We also stack only the 70 μm detected sources for comparison (hereafter, *"detected"*). Because the *all* stacks often appear to be dominated by the few 70 μm detected sources we generally use the *detected* and *undetected* stacks in our analysis.

In order to isolate trends between the IR emission from AGNs and other physical properties we further split the 'Restricted' sample (see §2.1.1) in terms of L_X ($= 10^{42-43}$ erg s^{-1}, $= 10^{43-44}$ erg s^{-1}), N_H ($< 10^{22}$ cm^{-2}, $= 10^{22-23}$cm^{-2}) and redshift ($z = 0.5 - 1.0$, $z = 1.0 - 2.0$).

2.2 Comparison Samples

In our analysis we compare the results from the sample of CDF-S X-ray AGNs/SBs to the IR properties of two archetypal AGNs, a sample of bright QSOs from Richards et al. (2006) and, most importantly, a sample derived from local ($z < 0.1$) AGNs in the *Swift*-BAT catalogue of hard X-ray detected AGNs (see §2.2.1, appendix and Tueller et al. 2008). For the latter we selected those AGNs that cover the same range of X-ray properties (i.e. L_X and N_H; see Fig. 2) as the CDF-S X-ray AGNs sample and also have archival *Spitzer*-IRS spectra and/or *IRAS* flux density measurements. The result is a sample that is *directly comparable* to the more distant CDF-S AGNs, but which has far superior IR data due to the relative proximity of the sources.

2.2.1 The Swift-BAT Sample

The *Swift* telescope is currently undertaking a survey of X-ray bright ($F_{14-195 \text{ keV}} \gtrsim 5 \times 10^{-11}$ erg s^{-1} cm^{-2}) AGNs using its onboard Burst Alert Telescope (BAT); the second data release (DR2) of this survey has recently been published in Tueller et al. (2008). As the BAT instrument is sensitive only to very hard X-rays (14-195 keV) this survey has resulted in a sample of local[5] AGNs that is largely unaffected by absorption (to $N_H < 10^{24}$ cm^{-2}). The L_X and N_H distributions of the 104 AGNs for which archival 2-10 keV data exist (Bassani et al. 1999; Winter et al. 2009) are comparable to the CDF-S sample (see Figs. 7 and 10 of Winter et al. 2009). Of these 104 AGNs, 61 have flux density measurements from all four *IRAS* bands (these 61 objects are hereafter referred to as the BAT/*IRAS* sample) which we convert to L_{IR} using Eqns. 2 and 3 in Table 1 of Sanders & Mirabel (1996). A search of the *Spitzer* archives reveals that 36 of the 104 AGNs with 2-10 keV data have *Spitzer*-IRS spectroscopy between 5.2–38 μm (these 36 objects are hereafter referred to as the BAT/IRS sample) which we use in conjunction with *IRAS* data to derive the expected observed 24 μm and 70 μm fluxes at the redshifts covered by the CDF-S sample. All of the AGNs in the BAT/IRS sample are also in the BAT/IRAS sample. See appendix for full details of the IRS/*IRAS* analysis.

On separating the BAT/IRS sample into SB and AGN dominated objects we find that the S_{70}/S_{24} ratio is able to discriminate between these two types of sources out to $z \approx 1.5$ (see shaded regions in Fig. 4 and appendix). Furthermore, we note that the 70 μm flux density can predict the infrared luminosities of all the BAT/IRS objects (i.e., both SB-dominated and AGN-dominated AGNs), as

well as the starburst galaxies described in Brandl et al. (2006), to within a factor of ≈ 3. This compares to a factor ≈ 12 uncertainty in L_{IR} using 24 μm flux densities alone (see appendix and Fig. A3).

In the plots that follow, we indicate the average IR properties of the BAT/IRS sample using red and blue lines for the AGN and SB dominated systems, respectively. Shading is used to indicate the range of MIR and FIR properties of the BAT/IRS sample.

2.2.2 NGC 1068, NGC 6240 and the QSO sample

In addition to the BAT/IRS sample we also compare the CDF-S AGNs with two well studied heavily obscured AGNs, NGC 1068 and NGC 6240. The former is regarded as the "quintessential" type-II AGN, showing evidence of a hidden broad line region in polarised light (e.g. Antonucci & Miller 1985); the latter is a heavily obscured AGN that is SB-dominated at infrared wavelengths and is often cited to characterise the properties of faint X-ray AGNs. The tracks for these AGNs were derived from archival *Spitzer*-IRS spectra following the same procedure as used for the BAT/IRS sample as outlined in the appendix.

Finally, we use the average QSO SED of Richards et al. (2006) to give an indication of the typical IR properties of luminous, unobscured type-I AGNs.

We stress that the comparison samples considered here do not cover the full range of SEDs seen in the general galaxy population. It is known, for example, that very strongly starbursting systems have larger S_{70}/S_{24} flux ratios than NGC 6240 (e.g. Arp 220). Furthermore, some quiescent galaxies are known to have low S_{70}/S_{24} flux ratios similar to those of AGNs in the BAT/IRS sample (see Alexander et al., in prep). However, our main aim here is to explore the IR emission of AGNs with X-ray properties comparable to the CDF-S AGNs, which excludes such extreme systems. We find that known starbursting systems, such as those presented in Brandl et al. (2006), all produce expected S_{70}/S_{24} flux ratios either consistent with or higher than those of the SB-dominated BAT/IRS AGNs, as indicated by the shaded region in Fig. A3.

3 RESULTS

In our analysis we investigate the IR properties of the CDF-S X-ray AGNs and SBs, including the S_{70}/S_{24} flux ratios, the IR luminosities and the IR−X-ray luminosity ratios. To aid in our analysis we compare the properties of the CDF-S X-ray sources with expectations based on the more detailed analysis of nearby AGNs with the same X-ray properties as the CDF-S sample (i.e., L_X; N_H). Since only a minority of CDF-S X-ray AGNs are detected at 70 μm, our analyses rely significantly on 70 μm stacking analyses and the 24 μm fluxes of individual sources.

3.1 Individual 70 μm detected sources

3.1.1 X-Ray properties and redshift distribution

In Fig. 1 we show the X-ray luminosity-redshift distribution for the CDF-S X-ray AGNs/SBs and highlight the 70 μm detected objects. As might be expected, there is a preference for bright X-ray AGNs to be detected at 70 μm. However, there are up to 2 orders of magnitude difference in L_X for 70 μm-detected sources at the same redshift, suggesting a large range of X-ray/IR luminosity ratios. As we show in Fig. 3, detection at 70 μm is strongly

---

[5] 135 of the 153 AGNs with measured redshifts in the BAT sample (presented in Tueller et al. 2008) have $z < 0.1$.
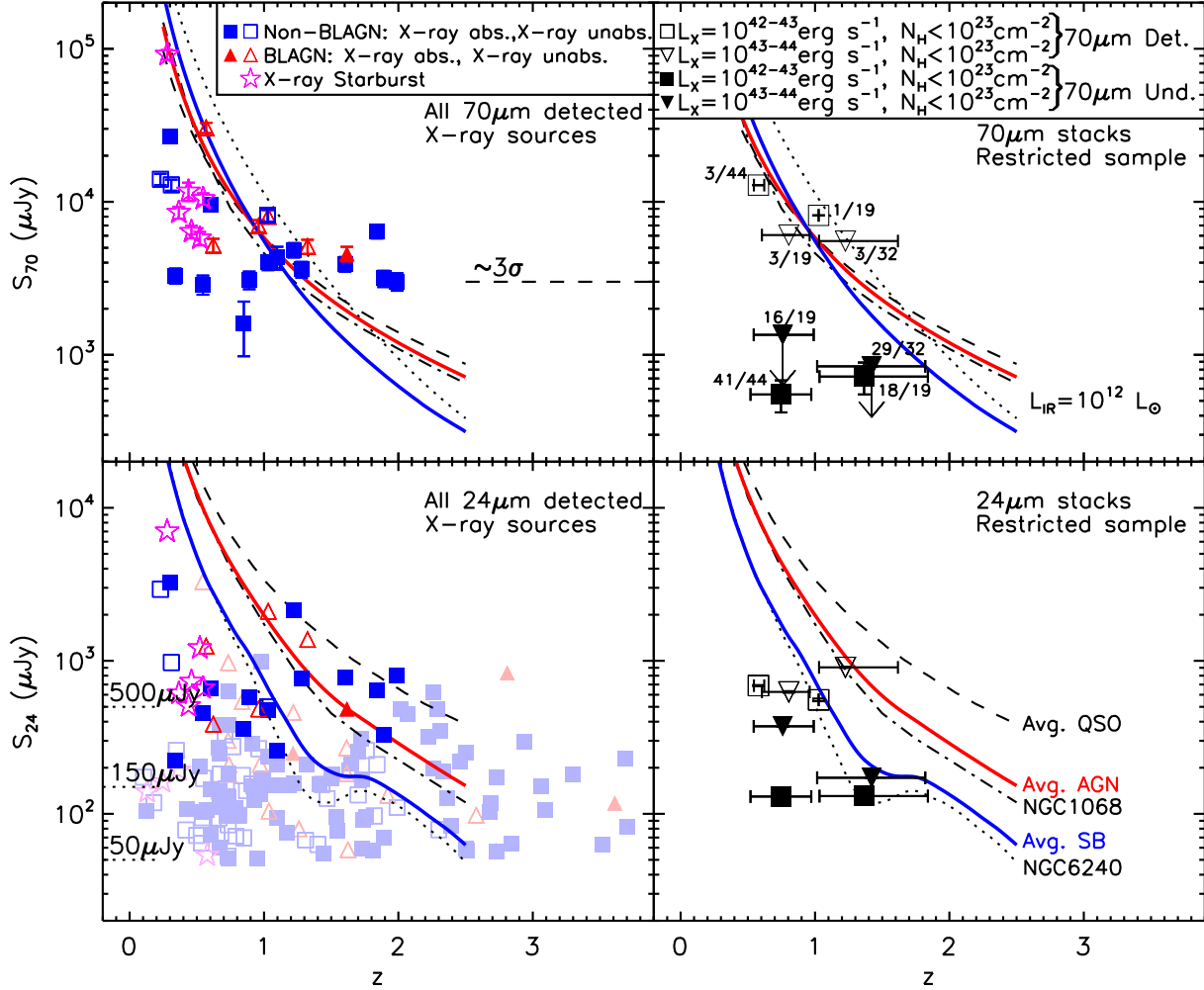
Figure 3. *Left Panels:* 70 µm (*top*) and 24 µm (*bottom*) flux densities of the CDF-S X-ray SBs and AGNs that are detected in both the 70 µm and 24 µm wavebands (strong colours) and only the 24 µm waveband (faint colours). *Right Panels:* The average 70 µm (*top*) and 24 µm (*bottom*) flux densities of the 70 µm *detected* and 70 µm *undetected* AGNs in the 'Restricted' sample, split according to L_X and z. These averages are derived from stacking analyses. The fractions indicate the number of AGNs in each stack as well as in the whole subsample. The five tracks in each panel show the expected flux densities of the comparison AGNs, normalised to $L_{IR}=10^{12}$ $L_\odot$, at $z = 0.25 - 2.5$.

dependent on the 24 µm flux density. None of the AGNs with $S_{24} < 200$ µJy, and fewer than a quarter (10/45; ≈22%) of those with $200 < S_{24}/\mu Jy < 500$, are detected at 70 µm. Conversely, the majority (19/28; ≈68%) of those AGNs with $S_{24} > 500$ µJy are detected at 70 µm.

The 70 µm detected sources span a broad range of X-ray properties. Of the 29 sources detected at both 70 µm and 24 µm, 15 (≈52%) are non-broad-line AGNs (non-BLAGNs), 6 (≈21%) are broad-line AGNs (BLAGNs) and 8 (≈28%) are X-ray detected SBs. These 70 µm detected sources comprise 15/218 (≈7%) of the non-BLAGNs, 6/34 (≈18%) of BLAGNs and 6/14 (≈43%) of the X-ray detected SBs; the bias toward the BLAGNs and X-ray detected SBs could be due to the BLAGNs and SBs having high L_X and large IR–X-ray luminosity ratios, respectively. The 70 µm detection of AGNs shows no apparent dependency on absorbing column density: for example, at $z < 1.5$, 6/17 (≈ 35%) 70 µm detected sources are unabsorbed ($N_H < 10^{22}$ cm^{-2}), 5/17 (≈ 29%) are absorbed ($N_H \approx 10^{22} - 10^{23}$ cm^{-2}) and 6/17 (≈ 35%) are heavily absorbed ($N_H > 10^{23}$ cm^{-2}).

3.1.2 *Distinguishing between SB and AGN dominated systems*

In Fig. 4 we show the S_{70}/S_{24} flux ratios of all of the CDF-S X-ray AGNs/SBs and compare them to the range expected for the BAT/IRS AGN sample and the well studied local AGNs and quasars; see section 2.2.1 and appendix. The S_{70}/S_{24} flux ratio provides an effective discrimination between those AGNs with AGN-dominated or SB-dominated IR SEDs to $z \approx 1 - 1.5$. Using the tracks derived for the BAT/IRS sample we find that 15/23 (≈65%) and 5/23 (≈22%) of the 70 µm detected CDF-S AGNs have S_{70}/S_{24} flux ratios consistent with SB-dominated and AGN-dominated systems, respectively; the remaining three 70 µm detected AGNs lie in regions of the $S_{70}/S_{24}-z$ plot that are consistent with either SB or AGN dominated systems. Ten (≈ 42%) of the 70 µm detected CDF-S AGNs have S_{70}/S_{24} flux ratios within a factor of 1.5 of the NGC 6240 track, five of which are X-ray absorbed and five of which are X-ray unabsorbed. The maximum S_{70}/S_{24} flux ratio of the 70 µm detected sources is 24.4 ± 1.9. This is marginally inconsistent with Papovich et al. (2007) who found 3/30 (≈10%) X-ray detected AGNs in their 70 µm selected sample with $S_{70}/S_{24} > 30$. However, the larger area covered by their
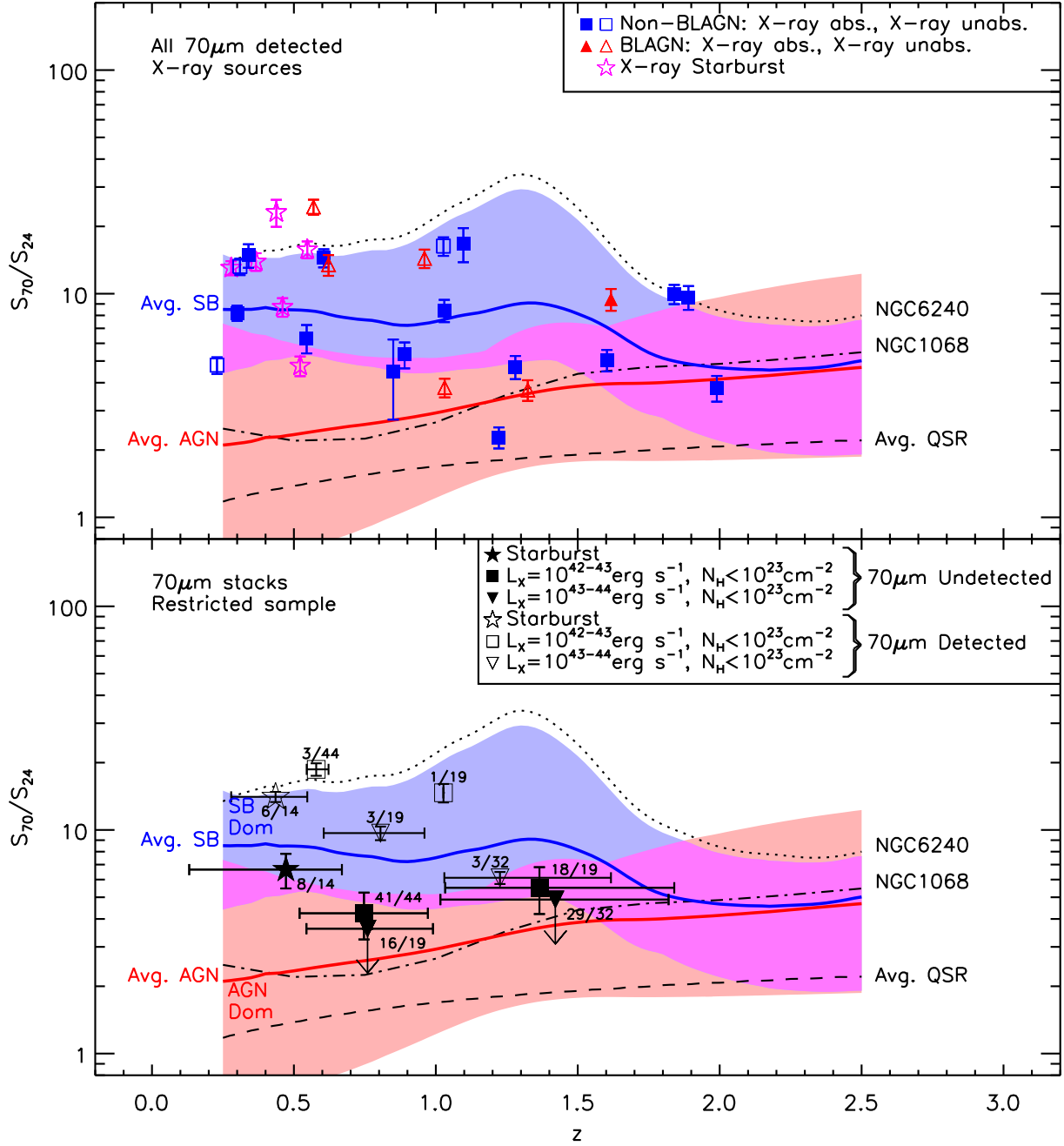
Figure 4. *Top:* S_{70}/S_{24} flux ratios of the CDF-S X-ray AGNs/SBs that are detected at 70 μm. *Bottom:* The average S_{70}/S_{24} flux ratios of the 70 μm *detected* and 70 μm *undetected* AGNs in the 'Restricted' sample, split according to L_X and z. These averages are derived from stacking analyses. The fractions indicate the number of AGNs in each stack as well as in the whole subsample. The five tracks indicate the expected S_{70}/S_{24} flux ratios of the comparison AGNs at $z = 0.25 - 2.5$; see §2.2 and appendix. The shaded regions indicate the range of expected S_{70}/S_{24} flux ratios of the AGNs in the BAT/IRS at $z = 0.25$–2.5.

survey increases the likelihood of finding rare AGNs with more extreme S_{70}/S_{24} flux ratios that are not represented by our comparison samples; see §2.2.

Among the 70 μm detected sources we find no difference in S_{70}/S_{24} flux ratio between BLAGNs and non-BLAGNs, nor between X-ray absorbed and X-ray unabsorbed AGNs (i.e., $N_H \geqslant 10^{22}$ cm^{-2} and $N_H < 10^{22}$ cm^{-2}, respectively), implying that the material that absorbs photons at X-ray and optical wavelengths is optically thin to rest frame MIR–FIR radiation, see §3.1.1. The average S_{70}/S_{24} flux ratios and redshifts of the absorbed (unabsorbed)

70 μm detected AGNs are $\overline{S_{70}/S_{24}} = 8.2 \pm 4.3$ (11.8 ± 7.3) and $\overline{z} = 1.1 \pm 0.6$ (0.76 ± 0.56)[6], respectively.

All six 70 μm detected X-ray SBs have S_{70}/S_{24} flux ratios consistent with that expected of SB-dominated systems. However, one of the SBs has a S_{70}/S_{24} flux ratio larger than that expected from the BAT/IRS sample and is typical of the extreme SB systems presented in Brandl et al. (2006), see Fig. A3. The 70 μm detected X-ray SBs also span the same range of S_{70}/S_{24} flux ratios as the

---

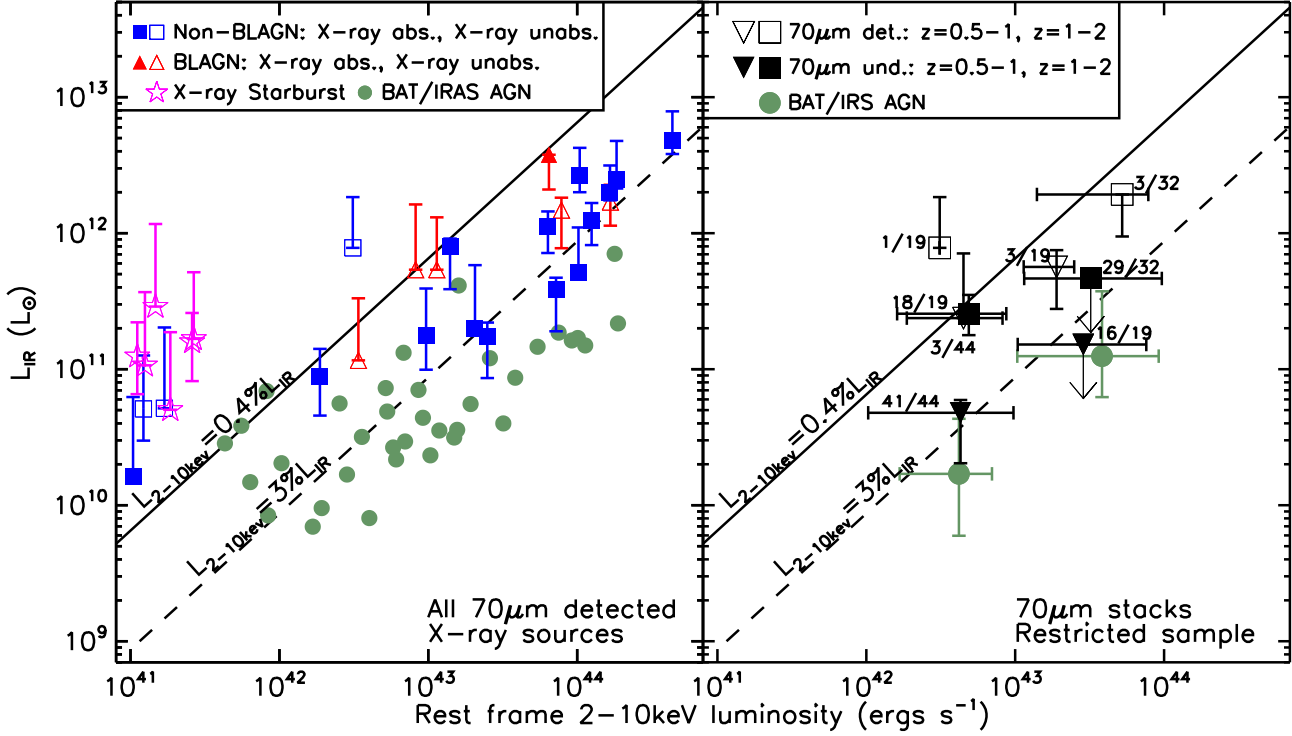[6] Given errors correspond to the standard deviation in the stacked flux

Figure 5. L_{IR} versus L_X of the 70 μm detected CDF-S X-ray AGNs/SBs (*left*) and the 70 μm *undetected* and 70 μm *detected* stacks of the 'Restricted' sample, separated according to redshift (*right*). In both plots, the vertical error bars indicate the range of L_{IR} produced by assuming the full range of tracks in Figs. 3 and 4 and horizontal error bars indicate the full range of L_X in each stack. For comparison we include the BAT/IRAS AGNs (see §2.2.1) and lines of constant L_{IR}/L_X for the average QSO of Elvis et al. (1994; $L_X = 3\%L_{IR}$) and the AGN-hosting submillimeter galaxies of Alexander et al. (2005; $L_X = 0.4\%L_{IR}$). For the average BAT/IRAS points we only include BAT/IRAS AGNs with X-ray properties matching those of the 'Restricted' sample (i.e., $L_X = 10^{42-44}$ erg s^{-1}, $N_H < 10^{23}$ cm^{-2}).

seven 70 μm detected X-ray AGNs that lie in the same redshift interval (i.e., $z = 0.2 - 0.7$), providing further evidence that these AGNs have SB-dominated IR SEDs.

3.1.3   IR fluxes and luminosities of individual, 70 μm-detected AGNs

Since we can provide a good characterisation of the basic IR SEDs of the 70 μm-detected CDF-S X-ray AGNs, we can accurately estimate their IR luminosities. We derive L_{IR} for the 70 μm detected sources by first selecting one of the five tracks plotted in Fig. 4 that best matches the S_{70}/S_{24} flux ratio of a given CDF-S X-ray AGN, then scaling its IR luminosity to reproduce S_{70} of the CDF-S source if observed at the same redshift. Estimating L_{IR} in this manner assumes that the IR SEDs of AGNs at the redshifts covered by the CDF-S observations are similar to those seen in the comparison AGN samples. We take some confidence that this is indeed the case as the range of S_{70}/S_{24} flux ratios of the 70 μm detected subsample is largely bounded by the tracks of our comparison sample.

In the left panel of Fig. 5 we show the L_{IR} of the 70 μm detected sample plotted as a function of L_X. We find no significant difference in L_{IR} between BLAGNs and non-BLAGNs or between X-ray absorbed and unabsorbed AGNs. This independence of L_{IR} on classification provides further supporting evidence that the material that absorbs photons at X-ray and optical wavelengths is optically thin to rest frame MIR–FIR radiation, see §§3.1.1 & 3.1.2. The 70 μm detected CDF-S X-ray AGNs are typically more IR luminous than their counterparts in the BAT/*IRAS* sample of local

AGN. This result may be due to the low sensitivity of the 70 μm observations, which could lead to a bias towards the detection of the most IR-luminous AGNs; indeed, the range of IR luminosities (≈ 2 orders of magnitude) for the CDF-S X-ray AGNs is narrower than the range of X-ray luminosities (≈ 3 orders of magnitude). Overall, the L_{IR}/L_X ratios of the 70 μm detected CDF-S AGNs/SBs span almost 2 orders of magnitude.

The 70 μm detected X-ray SBs have higher L_{IR}/L_X ratios than the majority (20/22; $\approx 91\%$) of the 70 μm detected X-ray AGNs. We find all three 70 μm detected X-ray AGNs with $L_X < 10^{41}$ erg s^{-1} have L_{IR}/L_X ratios and S_{70}/S_{24} flux ratios comparable to the 70 μm detected X-ray SBs (Tozzi et al. 2006 index: 525, 538, 575; see Table 1). However, two of these sources (index: 525, 538) have optical spectra consistent with AGNs (Szokoly et al. 2004) while the remainder (index: 575) has a flat X-ray spectral index in the deeper 2 Ms CDF-S catalogue ($\Gamma < 0.1$; Luo et al. 2008). While this confirms their classification as AGNs, it is clear that their IR SEDs are SB dominated.

As only a small fraction of the CDF-S X-ray AGN sample is detected at 70 μm we are unable to reliably constrain the IR properties of the majority of the CDF-S X-ray AGNs/SBs using the 70 μm data alone. To better characterise the IR properties for the majority of the CDF-S X-ray AGNs we therefore use stacking analyses.

3.2   24 μm and 70 μm stacking analysis

The advantage of stacking analyses is that it provides the average properties of sources that lie below the individual source detection

limit. However, naturally, information is lost on the fluxes of individual sources. We also stacked the 70 μm and 24 μm data following the procedure outlined in §2.1.4 and present the results in Table 2; although the majority of the CDF-S X-ray sources are detected at 24 μm, we stacked the 24 μm data to provide flux density constraints consistent with those obtained at 70 μm. For completeness, we report the results from stacking the whole sample as well as a range of subsamples (split into bins of L_X, N_H, z, 24 μm flux density, and object classification). As noted in §2.1.4, we stacked all X-ray sources in each subsample (*"all"*), and also stacked only the 70 μm detected objects (*"detected"*) and only the 70 μm undetected objects (*"undetected"*). The majority of our analyses will focus on the 'Restricted' sample to reduce selection and sensitivity biases (see §2.1.1).

All of the CDF-S X-ray sample is detected significantly in the 70 μm stacks, with an average flux density of S_{70}=4824 ± 210 μJy. Significant detections ($S/N > 3$) are also found from 70 μm stacking analyses for the majority of the subsamples; however, we note that only 9 ($\approx$ 50%) of the eighteen 70 μm *undetected* subsamples are significantly detected. From stacking the CDF-S X-ray sample in bins of 24 μm flux density (i.e. S_{24}=50-150 μJy, 150-500 μJy and $\geqslant$500 μJy), we find that the 70 μm flux density and the significance of the detection is positively correlated with the 24 μm flux density of the stacked sources, confirming our previous result for the 70 μm detected sources; see §3.1.

We find that when the 'Restricted' sample is stacked in bins of N_H and z (i.e., stacks 5, 6, 7 and 8 in Table 2) only one 70 μm *undetected* stack is detected at 70 μm at a significance > 3σ. The upper limits for these non-detections reveal no significant differences in the IR properties of these subsamples; they are all consistent with $S_{70}/S_{24}\approx$4 and $L_{IR}\approx 10^{11}$ L$_\odot$. The lack of any significant difference between these stacks may be interpreted as providing further tentative evidence that the material that absorbs X-rays is optically thin to rest frame MIR–FIR radiation, see §§3.1.1, 3.1.2 & 3.1.3. Similarly, none of the $L_X = 10^{43-44}$ erg s^{-1}, 70 μm *undetected* stacks (rows 13 and 14 of Table 2) are detected at > 3σ in either redshift bin ($z = 0.5$–1 and $z = 1$–2). However, in this case the upper limits *do* provide significant insight into the IR properties of the CDF-S X-ray AGNs, revealing that high L_X AGNs have, on average, warmer S_{70}/S_{24} flux ratios than their low L_X counterparts (as discussed in §3.2.1).

We proceed with the analysis of the stacked data following a similar procedure as outlined in §3.1 for the 70 μm detected sources.

3.2.1 SB/AGN contribution to the average IR emission of AGNs

In the lower panel of Fig. 4 we show the S_{70}/S_{24} flux ratios of the 'Restricted' subsamples split in terms of L_X and z (rows 11, 12, 13 and 14 of Table 2). We find that the average S_{70}/S_{24} flux ratios of all four 70 μm *undetected* stacks lie within the range of S_{70}/S_{24} flux ratios expected for the BAT/IRS AGNs out to $z \approx 2.5$, and run roughly parallel to the average AGN-dominated and average SB-dominated tracks (see §2.2.1 and appendix). The simplest interpretation of this result is that there is little change in the average IR colour with redshift for AGNs in both the $L_X = 10^{42-43}$ erg s^{-1} and $L_X = 10^{43-44}$ erg s^{-1} bins. However, the conservative upper limits on the S_{70}/S_{24} flux ratios of the $L_X = 10^{43-44}$ erg s^{-1} 70 μm *undetected* AGNs place them below those of the $L_X = 10^{42-43}$ erg s^{-1} 70 μm *undetected* AGNs in each redshift bin. Based on the BAT/IRS tracks this result suggests that the more X-ray luminous AGNs may have, on average, more AGN-dominated

IR SEDs than their lower L_X counterparts; however, deeper data will be required to confirm this result. However, we find that the stacks of the $L_X = 10^{42-43}$ erg s^{-1} AGNs lie in ambiguous regions of the $S_{70}/S_{24}-z$ plot, which limits the conclusions that can be directly derived on the relative contributions from AGN and SB activity to these stacks using the S_{70}/S_{24} flux ratios alone; in §4.1 we explore a variety of approaches to constrain the relative AGN and SB contributions using additional data.

3.2.2 Average IR fluxes and luminosities

The average IR luminosities of the stacked subsamples are calculated by taking the same approach as that used for the individual 70 μm detected sources (see §3.1.3). For those stacks with less than 3σ detections we use the nominal S_{70}/S_{24} flux ratio (rather than upper limits) when determining the closest match out of the five tracks considered; although we note that using upper limits to select the appropriate track changes the estimates of L_{IR} by less than 20%. In both redshift bins the nominal S_{70}/S_{24} flux ratios of the $L_X= 10^{42-43}$ erg s^{-1} and $L_X= 10^{43-44}$ erg s^{-1} 70 μm *undetected* stacks are most closely matched by the average AGN and average QSO SEDs, respectively. We note, however, that the 3 σ upper limits on the S_{70}/S_{24} flux ratios of stacked $L_X= 10^{43-44}$ erg s^{-1} AGNs are also consistent with the average AGN SED; see Fig. 4.

In Fig. 5 we plot the IR luminosity versus L_X for the CDF-S X-ray sources and the BAT/*IRAS* sample. In the case of the $L_X = 10^{42-43}$ erg s^{-1} *undetected* AGNs, we find that L_{IR} is larger by a factor of ≈ 5 for the $z = 1.0 - 2.0$ AGNs when compared to the $z = 0.5 - 1.0$ AGNs (L_{IR} =2.5×10^{11} L$_\odot$ and 5.0×10^{10} L$_\odot$, respectively), and a factor of $\approx$20 times larger than the average $42 <\log(L_X/\text{erg s}^{-1})< 43$, $N_H< 10^{23}$ cm^{-2} BAT/IRS AGN (i.e., at $z \approx 0$; L_{IR} =1.3×10^{10} L$_\odot$). This is in spite of these subsamples having almost the same average X-ray luminosities ($\overline{L_X}$ =4.9×10^{42}, 4.3×10^{42} erg s^{-1} and 3.7×10^{42} erg s^{-1} for $z = 1.0 - 2.0$, $z = 0.5 - 1.0$ and $z \approx 0$ AGNs, respectively). This difference corresponds to a factor of $4.7^{+10.2}_{-2.0}$ and $12.7^{+7.1}_{-2.6}$ increase in L_{IR}/L_X from $z = 0.5 - 1$ to $z = 1 - 2$ and from $z \approx 0$ to $z = 1.0 - 2.0$, respectively (these conservative errors correspond to the full range of IR luminosities derived using all five tracks in Fig. 4). The stacked data therefore suggest that the average L_{IR}/L_X ratio of $L_X = 10^{42-43}$ erg s^{-1} AGNs strongly evolves with redshift, as illustrated in Fig. 6. Although this result is based on stacking analyses, we show in §3.3 that we obtain the same result using 24 μm constraints for individual sources.

The 70 μm *undetected* stacks of the $L_X = 10^{43-44}$ erg s^{-1} AGNs at both $z = 0.5$–1 and $z = 1$–2 are not significantly detected, limiting the constraints that we can place on L_{IR} using the 70 μm data alone; the limits are $L_{IR} <1.5×10^{11}$ L$_\odot$ and $<4.6×10^{11}$ L$_\odot$ for the AGNs at $z = 0.5$–1 and $z = 1$–2, respectively (these upper limits include the uncertainty in the S_{70}–L_{IR} correction). However, because the upper limits on the S_{70}/S_{24} flux ratios of these stacks provide significant constraints to the range of potential matching BAT/IRS AGN SEDs we can estimate the average IR luminosities from the stacked 24 μm flux densities to a much higher degree of accuracy than would normally be the case (to within a factor of $\approx$3, rather than $\approx$12). This reduced uncertainty is based on the fact that the S_{70}/S_{24} flux ratios of the $L_X = 10^{43-44}$ erg s^{-1} AGN stacks restricts us to AGN-dominated BAT/IRS SEDs, which all have similar S_{24}–L_{IR} ratios. Using the stacked 24 μm flux density we obtain L_{IR}=5.6×10^{10} L$_\odot$ and 1.2×10^{11} L$_\odot$ for the $L_X = 10^{43-44}$ erg s^{-1} AGNs in the $z = 0.5 - 1.0$ and $z = 1.0 - 2.0$ redshift bins, respectively, corresponding to a factor of $\approx$2 increase between these redshift ranges. For comparison, the aver-
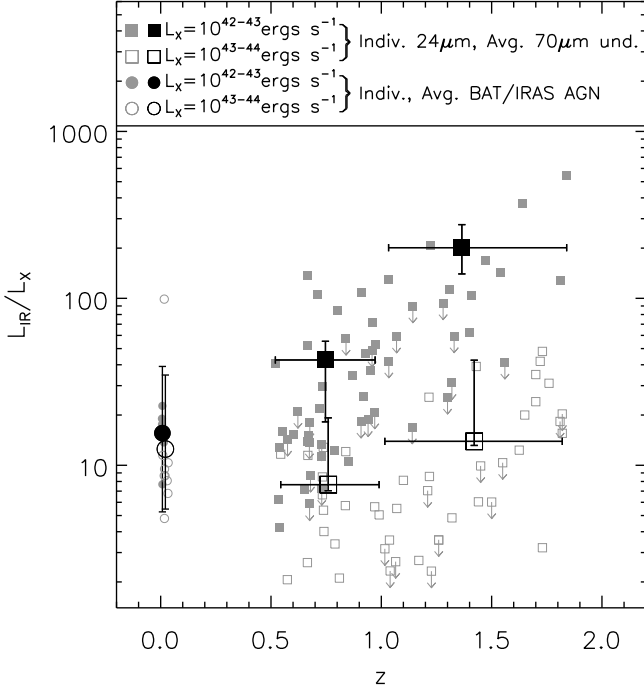
Figure 6. L_{IR}/L_X versus redshift for the stacked 70 μm *undetected* sources in the 'Restricted' sample of CDF-S X-ray AGNs, separated according to L_X (black squares). Vertical error bars indicate the range of L_{IR}/L_X produced by assuming the various tracks in Figs. 3 and 4. Small, grey squares indicate the L_{IR}/L_X ratios of each X-ray AGN in the 'Restricted' sample derived from their 24 μm flux densities, assuming the Average AGN and Average QSO SEDs for the $L_X = 10^{42-43}$ erg s^{-1} and $L_X = 10^{43-44}$ erg s^{-1} AGNs, respectively (see §3.3). For those sources undetected at 24 μm we derive upper limits by assuming a 24 μm flux density limit of 50 μJy. For comparison we include the individual and average L_{IR}/L_X ratios of the BAT/IRAS sample, separated according to L_X (vertical error bars indicate the standard deviation of L_{IR}/L_X of the BAT/IRS sample). Both the stacking analysis and the individual 24 μm detections clearly show a consistent increase in the L_{IR}/L_X ratio of $L_X = 10^{42-43}$ erg s^{-1} AGN from $z \approx 0$ to $z = 1-2$.

age L_{IR} of $L_X = 10^{43-44}$ erg s^{-1} AGNs in the $z \approx 0$ BAT/IRS sample is 1.2×10^{11} L$_\odot$. Given the average X-ray luminosities of these AGNs (i.e., $\overline{L_X} = 3.8 \times 10^{43}$ erg s^{-1}, 2.9×10^{43} erg s^{-1} and 3.2×10^{43} erg s^{-1} for the $z \approx 0$, $z = 0.5-1$ and $z = 1-2$ AGNs, respectively), we constrain the change in L_{IR}/L_X to a factor of $\approx 1.8^{+4.2}_{-1.0}$ between $z = 0.5-1$ and $z = 1-2$ and to a factor of $\approx 1.2^{+2.6}_{-0.8}$ between $z \approx 0$ and $z = 1-2$, both of which are consistent with no evolution; see Fig. 6.

A number of recent studies have shown that the MIR emission of AGNs can be used as a good proxy for their intrinsic luminosities (e.g. Krabbe et al. 2001; Lutz et al. 2004; Maiolino et al. 2007; Horst et al. 2008). Understanding how the X-ray–MIR relationship changes with redshift would be very useful for detecting potentially heavily obscured AGNs (e.g., Daddi et al. 2007; Fiore et al. 2008; Georgantopoulos et al. 2008). However, previous X-ray–MIR studies of AGNs have been limited to extremely high luminosity sources (i.e., $\overline{L_X} = 3 \times 10^{45}$ erg s^{-1}) at redshifts beyond $z \approx 0.3$. Using the results from our stacking analyses we can constrain the X-ray–MIR luminosity ratios (hereafter we focus on $\nu L_\nu(6\mu m)/L_X$) of more typical, distant AGNs found in deep, multi-wavelength surveys. At $z \approx 0$ the $\nu L_\nu(6\mu m)/L_X$ ratios of the Average AGN and Average QSO SEDS are consistent

with Lutz et al. (2004) (i.e., ≈ 3 and ≈ 2, respectively)[7]. To calculate the $\nu L_\nu(6\mu m)/L_X$ ratios of the CDF-S AGNs we assume the same SEDs as those used to derive their L_{IR}/L_X ratios (i.e., Average AGN and Average QSO for $L_X = 10^{42-43}$ erg s^{-1} and $L_X = 10^{43-44}$ erg s^{-1} AGNs, respectively). We therefore find that the average $\nu L_\nu(6\mu m)/L_X$ ratios of $L_X = 10^{42-43}$ erg s^{-1} AGNs increase from ≈ 3 at $z \approx 0$ to ≈ 10 and ≈ 43 at $z = 0.5-1$ and $z = 1-2$, respectively. By contrast, the average $\nu L_\nu(6\mu m)/L_X$ ratios of $L_X = 10^{43-44}$ erg s^{-1} AGNs remain largely unchanged to $z \approx 2$ (i.e., $\nu L_\nu(6\mu m)/L_X \approx 1-2$). Our data therefore suggest that deep IR observations can be used as a reliable method of identifying intrinsically bright (i.e., $L_X = 10^{43-44}$ erg s^{-1}), potentially Compton-thick AGNs. However, we urge caution when using either the L_{IR}/L_X or $\nu L_\nu(6\mu m)/L_X$ ratios to locate less luminous obscured AGNs (i.e., $L_X \lesssim 10^{43}$ erg s^{-1}) unless other indicators of luminous AGN activity are present (e.g., emission line spectra; see Alexander et al. 2008).

---

[7] We also note that the $\nu L_\nu(10.5\mu m)/L_X$ ratios of the Average AGN and Average QSO at $z \approx 0$ are largely consistent with the relationship presented in Krabbe et al. (2001) (i.e., $\nu L_\nu(10.5\mu m)/L_X \approx 2.5$ and ≈ 1.9, respectively).

Table 1. The 30 X-ray detected sources with $> 3\sigma$ detection at 70 μm.

(1) T06	(2) A03	(3) Name	(4) RA	(5) Dec	(6) z	(7) z flag	(8) $\log(L_X)$ (ergs s^{-1})	(9) N_H (10^{22} cm^{-2})	(10) S_{70} (μJy)	(11) S_{24} (μJy)	(12) $\frac{S_{70}}{S_{24}}$	(13) L_{IR} ($L_\odot$)	(14) Classification
7	312	J033301.8-275818	53.2574	-27.9718	1.840	0.6	44.64	3.57	6370 ± 620	640 ± 11	9.96 ± 0.99	12.7	Abs. Non-BLAGN
29	240	J033239.0-275701	53.1626	-27.9505	0.300	0.9	42.98	5.32	26600 ± 2100	3239 ± 11	8.20 ± 0.64	11.2	Abs. Non-BLAGN
31	230	J033237.9-275213	53.1577	-27.8704	1.603	3.0	44.22	1.79	3920 ± 430	777.4 ± 9.3	5.05 ± 0.56	12.3	Abs. Non-BLAGN
31	230	J033237.9-275213	53.1577	-27.8704	1.603	3.0	44.22	1.79	3920 ± 430	248.3 ± 9.3	15.8 ± 1.8	12.2	Abs. Non-BLAGN
36	204	J033233.1-274548	53.1379	-27.7634	1.030	0.5	43.15	1.73	4020 ± 440	477 ± 13	8.42 ± 0.96	11.9	Abs. Non-BLAGN
44	173	J033226.6-274036	53.1108	-27.6767	1.031	3.0	43.89	0.08	8010 ± 770	2107 ± 15	3.80 ± 0.37	12.2	Unabs. BLAGN
46	163	J033225.3-274219	53.1052	-27.7054	1.617	3.0	43.81	1.08	4580 ± 500	485 ± 13	9.4 ± 1.1	12.6	Abs. BLAGN
51	118	J033217.3-275221	53.0719	-27.8728	1.097	3.0	44.01	22.42	4340 ± 740	259.2 ± 8.6	16.7 ± 2.9	11.7	Abs. Non-BLAGN
52	117	J033217.2-274304	53.0718	-27.7178	0.569	3.0	42.91	0.04	30500 ± 2300	1247 ± 10	24.4 ± 1.9	11.7	Unabs. BLAGN
56	88	J033213.3-274241	53.0554	-27.7115	0.605	3.0	43.31	1.62	9620 ± 860	665 ± 16	14.5 ± 1.3	11.3	Abs. Non-BLAGN
69	38	J033201.5-274138	53.0063	-27.6941	0.850	0.4	43.40	3.20	1600 ± 620	356.9 ± 8.9	4.5 ± 1.8	11.2	Abs. Non-BLAGN
72	30	J033158.3-275043	52.9931	-27.8453	1.990	0.5	44.26	7.77	3020 ± 400	796.2 ± 9.1	3.79 ± 0.50	12.4	Abs. Non-BLAGN
77	311	J033301.7-274543	53.2570	-27.7620	0.622	3.0	42.53	0.44	5190 ± 540	385.7 ± 9.1	13.5 ± 1.4	11.1	Unabs. BLAGN
78	193	J033230.1-274524	53.1256	-27.7568	0.960	3.0	43.06	<0.19	6960 ± 640	484 ± 12	14.4 ± 1.4	11.7	Unabs. BLAGN
98	260	J033244.3-275142	53.1846	-27.8618	0.279	3.0	41.17	<0.02	91600 ± 6700	7020 ± 11	13.05 ± 0.95	11.5	Unabs. Starburst
122	295	J033257.7-274549	53.2404	-27.7636	2.100	0.5	43.47	2.58	4030 ± 460	-	-	-	Abs. Non-BLAGN
152	302	J033259.4-274859	53.2476	-27.8165	1.280	0.6	43.80	19.41	3620 ± 430	769 ± 11	4.71 ± 0.56	12.0	Abs. Non-BLAGN
155	60	J033208.0-274240	53.0335	-27.7111	0.545	3.0	42.27	3.59	2880 ± 410	455 ± 10	6.33 ± 0.92	10.9	Abs. Non-BLAGN
175	284	J033252.0-274437	53.2165	-27.7438	0.522	3.0	41.41	<5.26	5770 ± 580	1213 ± 11	4.76 ± 0.48	11.2	Abs. Starburst
206	109	J033216.3-273930	53.0678	-27.6586	1.324	3.0	44.22	0.13	5100 ± 540	1376 ± 12	3.71 ± 0.39	12.2	Unabs. BLAGN
242	285	J033251.9-274229	53.2164	-27.7083	1.027	3.0	42.49	0.72	8150 ± 750	500 ± 11	16.3 ± 1.5	11.9	Unabs. Non-BLAGN
253	131	J033220.1-274448	53.0839	-27.7467	1.890	1.9	44.02	73.51	3160 ± 380	327.20 ± 0.20	9.6 ± 1.2	12.4	Abs. Non-BLAGN
268	278	J033249.3-274050	53.2056	-27.6806	1.222	3.0	44.10	80.44	4850 ± 520	2127 ± 16	2.28 ± 0.25	12.1	Abs. Non-BLAGN
525	129	J033219.9-274123	53.0828	-27.6899	0.229	3.0	41.09	0.00	14000 ± 1200	2932 ± 17	4.79 ± 0.41	10.7	Unabs. Non-BLAGN
538	65	J033208.6-274649	53.0359	-27.7803	0.310	3.0	41.23	0.51	12900 ± 1100	973 ± 14	13.2 ± 1.1	10.7	Unabs. Non-BLAGN
553	292	J033256.8-275318	53.2366	-27.8885	0.366	3.0	41.27	<0.17	8520 ± 770	612.3 ± 7.1	13.9 ± 1.3	10.7	Unabs. Starburst
567	236	J033238.9-274732	53.1620	-27.7925	0.460	3.0	41.05	<0.16	6370 ± 600	730.9 ± 8.9	8.72 ± 0.83	11.1	Unabs. Starburst
575	115	J033217.2-274922	53.0715	-27.8230	0.340	3.0	41.02	1.90	3290 ± 370	221.5 ± 9.5	14.8 ± 1.8	10.2	Abs. Non-BLAGN
577	224	J033236.3-274933	53.1512	-27.8258	0.547	3.0	41.42	<0.14	10470 ± 890	664 ± 10	15.8 ± 1.4	11.2	Unabs. Starburst
608	318	J033304.0-275027	53.2665	-27.8409	0.890	3.0	43.86	150.00	3090 ± 410	578.0 ± 9.3	5.34 ± 0.71	11.6	Abs. Non-BLAGN
646	266	J033245.2-274724	53.1884	-27.7903	0.438	3.0	41.10	<0.19	11700 ± 1600	507.2 ± 8.6	23.1 ± 3.2	11.0	Unabs. Starburst

NOTES: (1) Source index from Tozzi et al. (2006). (2) Source index from Alexander et al. (2003). (3) Source name. (4-5) X-ray position (J2000). (6) Source redshift. (7) Redshift flag. (8) Intrinsic (i.e., corrected for absorption) $2 - 10 keV$ luminosity. (9) Column density in units of 10^{22}cm^{-2}. (10) 70 μm flux. (11) 24 μm flux. (14) 70/24 μm flux ratio. (13) L_{IR} derived from the 70 μm flux using the method described in the text. (14) Classification from Bauer et al. (2004). Information in cols. (1),(3)-(9) is taken from Tozzi et al. (2006).

Table 2. Descriptions and average properties of the AGN and SB stacks.

(1) Index	(2) Description	(3) N All	Det.	Und.	(4) Mean z All	Det.	Und.	(5) log($\overline{L_X}$) (ergs s^{-1}) All	Det.	Und.	(6) Stacked S_{70} (μJy) All	Det.	Und.	(7) Stacked S_{24} (μJy) All	Det.	Und.	(8) L_{IR} ($L_\odot$) All	Det.	Und.
1	*Starbursts*	14	6	8	0.46	0.44	0.47	41.41	41.26	41.49	**9960 ± 500**	**22400 ± 1200**	**630 ± 110**	736.8	1592.9	94.7	11.0	11.3	10.1
2	$z < 1\ L_X = 10^{41-42}$	25	3	22	0.43	0.29	0.45	41.60	41.12	41.64	**1540 ± 160**	**10070 ± 550**	380 ± 170	235.7	1183.5	106.4	10.4	10.8	<10.5
3	$z > 3$	12	0	12	3.52	-	3.52	44.31	-	44.31	280 ± 180	-	280 ± 180	127.5	-	127.5	-	-	-
4	*BLAGN*	34	6	28	1.54	1.02	1.65	43.94	43.74	43.97	2050 ± 150	**10050 ± 450**	330 ± 160	419.3	957.3	304.1	12.0	12.3	<11.9
5	$z = 0.5 - 1\ L_X = 10^{42-44}\ N_H < 10^{22}$	32	3	29	0.74	0.72	0.74	43.10	42.88	43.12	**2180 ± 170**	**14200 ± 830**	**940 ± 170**	301.6	820.2	247.9	11.2	11.7	10.9
6	$z = 1 - 2\ L_X = 10^{42-44}\ N_H < 10^{22}$	19	2	17	1.38	1.03	1.42	43.39	43.61	43.35	**1230 ± 160**	**8080 ± 540**	420 ± 170	265.0	1156.6	160.1	11.7	12.2	<11.7
7	$z = 0.5 - 1\ L_X = 10^{42-44}\ N_H = 10^{22-23}$	31	3	28	0.75	0.67	0.76	42.99	43.20	42.96	**750 ± 140**	**4700 ± 380**	330 ± 150	180.0	494.0	146.3	10.8	11.4	<10.9
8	$z = 1 - 2\ L_X = 10^{42-44}\ N_H = 10^{22-23}$	32	2	30	1.38	1.32	1.39	43.35	43.59	43.33	**680 ± 140**	**4300 ± 330**	440 ± 150	174.4	480.3	154.0	11.4	12.3	<11.7
9	$z = 0.5 - 1\ L_X = 10^{42-44}\ N_H < 10^{23}$	63	6	57	0.74	0.69	0.75	43.05	43.07	43.05	**1440 ± 110**	**9450 ± 460**	**600 ± 110**	241.7	657.1	198.0	11.0	11.5	10.7
10	$z = 1 - 2\ L_X = 10^{42-44}\ N_H < 10^{23}$	51	4	47	1.38	1.18	1.40	43.36	43.60	43.34	**920 ± 110**	**6190 ± 320**	470 ± 120	208.1	818.5	156.2	11.5	12.3	11.2
11	$z = 0.5 - 1\ L_X = 10^{42-43}\ N_H < 10^{23}$	44	3	41	0.74	0.58	0.75	42.63	42.65	42.63	**1390 ± 130**	**12850 ± 820**	550 ± 130	167.8	688.3	129.7	11.0	11.4	10.7
12	$z = 1 - 2\ L_X = 10^{42-43}\ N_H < 10^{23}$	19	1	18	1.35	1.03	1.37	42.68	42.49	42.69	**1110 ± 170**	**8150 ± 750**	**720 ± 170**	153.0	555.6	130.6	11.7	11.9	11.4
13	$z = 0.5 - 1\ L_X = 10^{43-44}\ N_H < 10^{23}$	19	3	16	0.77	0.81	0.76	43.43	43.28	43.46	**1510 ± 200**	**6060 ± 410**	660 ± 230	413.1	625.9	373.2	11.1	11.8	<11.2
14	$z = 1 - 2\ L_X = 10^{43-44}\ N_H < 10^{23}$	32	3	29	1.40	1.23	1.42	43.53	43.72	43.51	**870 ± 140**	**5540 ± 340**	390 ± 150	240.9	906.1	172.1	11.5	12.3	<11.7
15	$S_{24} = 50\mu Jy - 150\mu Jy$	68	0	68	1.40	-	1.40	43.73	-	43.73	260 ± 90	-	260 ± 90	113.2	-	113.2	<11.4	-	<11.4
16	$S_{24} = 150\mu Jy - 500\mu Jy$	68	10	58	1.37	1.00	1.44	43.75	43.52	43.78	**1263 ± 97**	**4420 ± 180**	**720 ± 110**	285.9	456.9	256.4	11.7	11.9	11.5
17	$S_{24} \geqslant 500\mu Jy$	20	13	7	1.10	1.01	1.27	44.02	44.01	44.04	**7040 ± 230**	**10120 ± 300**	**1330 ± 320**	1113.4	1199.7	953.0	12.2	12.3	11.6
18	$S_{24} \geqslant 50\mu Jy$	156	23	133	1.35	1.01	1.41	43.79	43.86	43.77	**1570 ± 66**	**7640 ± 190**	**520 ± 70**	316.7	876.8	219.9	11.7	12.1	11.3

NOTES: (1) Stack index. (2) Stack description. (3) The numbers of CDF-S AGNs/SBs in each stack. (4) Mean redshift of the sources in each stack. (5) Logarithm of the mean, absorption corrected X-ray luminosity of the sources in each stack. (7) Stacked 70 μm flux density per source. (8) Stacked 24 μm flux density per source. (9) Infrared luminosity per source (over the 8-1000 μm interval), derived from the 70 μm flux density. Upper limits include the uncertainty on the S_{70}–L_{IR} correction. We do not calculate L_{IR} for stack (4), $z > 3$ AGN, as the mean redshift is beyond the range of the tracks derived from the BAT/IRS sample.

3.3 24 μm Properties

The results on the L_{IR}/L_X ratios in §3.2 were based on stacking analyses, which could be biased by a few bright 70 μm undetected sources. Since the majority of the CDF-S X-ray AGNs are individually detected at 24 μm, we can perform a complementary test of our results that does not rely significantly on stacking analyses. The advantage of this approach is that we can assess the range of L_{IR} for the X-ray AGNs, although there can be considerable uncertainty in the conversion between 24 μm flux density and L_{IR} for individual objects; see Fig. 3. However, as we show in Fig. 3, provided the average SED is not predominantly starburst dominated, then we can predict the average L_{IR}/L_X ratio, on the basis of the 24 μm data, to within a factor of ≈ 3; on the basis of Fig. 4, the average SEDs are AGN dominated, and would be increasingly so if the stacked 70 μm flux is dominated by bright undetected sources. Furthermore, so long as the average SEDs of the $z = 0.5$–1 AGNs are the same as the $z = 1$–2 AGNs, then we can accurately assess the relative change in L_{IR}/L_X between these redshifts; we provide evidence in §4.1 that this does appear to be the case. To convert from 24 μm flux densities to L_{IR} we use the same SEDs as assumed when calculating L_{IR} from the stacked 70 μm flux densities (i.e., Average AGN and Average QSO for the $L_X = 10^{42-43}$ erg s^{-1} and 10^{43-44} erg s^{-1} AGNs, respectively; see §3.2.2). For those AGNs that are undetected at 24 μm we calculated upper limits on L_{IR} assuming $S_{24} = 50$ μJy; however, we note that this assumption has a small effect on our average results (i.e., $\overline{L_{IR}/L_X}$ only changes by $\approx 35\%$ even if we assume extreme upper limits of $S_{24} = 0$ μJy). The average L_{IR}/L_X ratios derived from the 24 μm fluxes are given in Table 1.

We include in Fig. 6 the individual L_{IR}/L_X ratios calculated using the L_{IR} values derived from 24 μm fluxes of the 70 μm *undetected* AGNs in the 'Restricted' sample. For both the $L_X = 10^{42-43}$ erg s^{-1} and $L_X = 10^{43-44}$ erg s^{-1} AGNs the mean L_{IR}/L_X ratios increase with redshift by factors of ≈ 4.5 and ≈ 1.8, respectively. These results are in qualitative agreement with those obtained from the 70 μm stacks and indicates that the stacks are not dominated by a few extreme sources; these results are also confirmed by the median L_{IR}/L_X ratios presented in Table 3. However, we note that there is a factor of ≈ 2 offset between the L_{IR}/L_X ratios derived from the 70 μm stacks and individual 24 μm flux densities. This is caused by the difference between the S_{70}/S_{24} flux ratios of the 70 μm *undetected* stacks and the assumed SEDs (see Fig. 4) and disappears if we assume the SEDs of the two individual BAT/IRS AGNs that most closely reproduce (at both redshift bins) the S_{70}/S_{24} flux ratios of the 70 μm *undetected* $L_X = 10^{42-43}$ erg s^{-1} and 10^{43-44} erg s^{-1} stacks: NGC 1275 and Mrk 290, respectively.

4 DISCUSSION

We have provided multiple lines of evidence for an increase in the L_{IR}/L_X ratio for AGNs over the redshift range $z = 0 - 2$, with $L_X = 10^{42-43}$ erg s^{-1} AGNs ≈ 5 times more infrared luminous at $z = 1 - 2$ than at $z = 0.5 - 1$ (and ≈ 20 times more infrared luminous than at $z \approx 0$). The evidence for an increase in L_{IR} for $L_X = 10^{43-44}$ erg s^{-1} AGNs is less conclusive: a factor of ≈ 2 between $z = 0.5 - 1$ and $z = 1 - 2$ and no change from $z \approx 0$ and $z = 1 - 2$.

These results provide new insight into the production of IR emission from distant AGNs and lead to a number of questions, which we address below.

4.1 What is driving the increase in L_{IR}?

The L_{IR}/L_X ratio for the $L_X = 10^{42-43}$ erg s^{-1} AGNs at $z = 1 - 2$ is higher than that found for lower redshift X-ray AGNs; see Table 3. However, the L_{IR}/L_X ratio for the $L_X = 10^{42-43}$ erg s^{-1} AGNs is broadly consistent with $z \approx 2$ submillimeter emitting galaxies (SMGs) hosting AGN activity ($L_{FIR}/L_X \approx 250$; Alexander et al. 2005). On the basis of sensitive *Spitzer*-IRS spectroscopy, the large L_{FIR}/L_X ratio from AGN-hosting SMGs appears to be due to intense star-formation activity, with an average contribution to L_{FIR} from AGN activity of $\approx 10\%$ (e.g., Pope et al. 2008; Menéndez-Delmestre et al. 2007, 2009). Can the increase in the average L_{IR}/L_X ratio of the $z = 1 - 2$ AGNs also be due to increased star-formation activity?

There is no clear relative offset between the stacked S_{70}/S_{24} flux ratio and the AGN-dominated track for the $L_X = 10^{42-43}$ erg s^{-1} AGNs over the redshift range $z = 0.5 - 2$, appearing to suggest that the relative AGN/SB contribution to L_{IR} has not changed with redshift. If we derive the relative AGN/SB contribution to the stacked S_{70}/S_{24} using the average AGN and SB tracks, then we estimate $\approx 60\%$ and $\approx 70\%$ of the AGNs with $L_X = 10^{42-43}$ erg s^{-1} have AGN-dominated SEDs at $z = 0.5 - 1$ and $z = 1 - 2$, respectively; by comparison, the stacked S_{70}/S_{24} of the $L_X = 10^{43-44}$ erg s^{-1} AGNs suggest $\approx 100\%$ have AGN-dominated SEDs over the full redshift range. However, since it is difficult to unambiguously determine the relative AGN/SB contribution to L_{IR} from the S_{70}/S_{24} flux ratios at $z > 1.5$ (see Fig. 4), this result should be considered tentative.[8] Therefore, we explore below the implication of our results assuming both an increase in star formation and AGN activity.

If the observed increase in L_{IR} is attributed to star-formation it would imply a significantly higher (i.e., a factor of ≈ 5) ratio between star-formation and black hole growth at $z = 1 - 2$ compared to $z = 0.5 - 1$, and a factor of ≈ 13 increase between $z \approx 0$ and $z = 1 - 2$. Whether this has significant implications for the black-hole–bulge mass relationship depends on the location of the star-formation in the host galaxy and on the AGN fraction (i.e., the duty cycle of black-hole growth). For example, using Eqn. 4 of Kennicutt (1998) to derive the star-formation rate from L_{IR} and deriving the mass accretion rate from L_X, we estimate that the ratio between the average star-formation and mass accretion rate is ≈ 500 in the $z = 1 - 2$ AGNs, which is consistent with the black-hole to bulge mass ratio observed in the local universe (i.e., ≈ 800; McLure & Dunlop 2002; Marconi & Hunt 2003). This would appear to suggest a closer relationship between black-hole and stellar growth at $z = 1 - 2$ than found at $z = 0.5 - 1$, where the average star-formation and mass accretion rate would be ≈ 100 (and ≈ 30 at $z \approx 0$), based on the same assumptions as above. However, these different results could be reconciled if the AGN fraction is higher at higher redshifts or if the majority of the star formation at higher redshifts is occurring in the galaxy disk rather than the galaxy bulge, or vice-versa.

If, however, the increase in the L_{IR}/L_X ratio is due to the AGN, it would imply that a larger fraction of the intrinsic emis-

---

[8] We note that we also find a similar fraction ($\approx 30\%$) of $L_X = 10^{42-43}$ erg s^{-1} AGNs at $z = 1 - 2$ have IRAC 3.6–8.0 μm colours suggesting AGN-dominated SEDs (based on Stern et al. 2005) as that found for $L_X = 10^{42-43}$ erg s^{-1} AGNs at $z = 0.5 - 1$. This also suggests that the relative AGN/SB contribution for $L_X = 10^{42-43}$ erg s^{-1} AGNs is constant with redshift but we caution that this result is based on shorter-wavelength data than used to derive L_{IR}.

Table 3. Average properties of the CDF-S X-ray AGNs in the 70 μm *undetected*, 'Restricted' sample (see §2.1.1). N_{all} is the number of AGNs detected in each bin and N_{det} is the number of these that are detected at 24 μm. $\overline{z}$ is the mean redshift of the AGNs in each subsample and $\log(\overline{L_X})$ and $\log(\widetilde{L_X})$ indicate their mean and median L_X. We provide the mean L_{IR}/L_X ratios derived from the 70 μm and 24 μm stacks (assuming the Average AGN and Average QSO SEDs for the $L_X = 10^{42-43}$ erg s^{-1} and $L_X = 10^{43-44}$ erg s^{-1} subsamples, respectively) as well as the mean and median L_{IR}/L_X ratios derived from the individual 24 μm flux densities. Finally, we provide the mean and median L_{IR}/L_X derived from the individual 24 μm flux densities assuming the two BAT/IRAS tracks that most closely match the S_{70}/S_{24} flux ratios of the $L_X = 10^{42-43}$ erg s^{-1} and $L_X = 10^{43-44}$ erg s^{-1} subsamples at both $z = 0.5 - 1$ and $z = 1 - 2$: NGC 1275 and Mrk 290, respectively.

	N_{all}	N_{det}	$\overline{z}$	$\log(\overline{L_X})$	$\log(\widetilde{L_X})$	Stacks $\frac{\overline{L_{IR,70}}}{L_X}$	$\frac{\overline{L_{IR,24}}}{L_X}$	Avg. AGN/QSO $\frac{\overline{L_{IR,24}}}{L_X}$	$\frac{\widetilde{L_{IR,24}}}{L_X}$	BAT/IRAS closest match $\frac{\overline{L_{IR,24}}}{L_X}$	$\frac{\widetilde{L_{IR,24}}}{L_X}$
$z = 0.5 - 1, L_X = 10^{42-43}$erg/s	41	28	0.7	42.6	42.6	42.7	26.2	24.9	18.0	28.1	20.3
$z = 1 - 2, L_X = 10^{42-43}$erg/s	19	10	1.4	42.7	42.6	201.2	133.3	112.6	80.2	164.2	100.2
$z = 0.5 - 1, L_X = 10^{43-44}$erg/s	16	15	0.8	43.5	43.4	< 17.4	7.7	6.4	5.3	8.9	7.7
$z = 1 - 2, L_X = 10^{43-44}$erg/s	30	19	1.4	43.5	43.4	< 35.1	13.9	11.4	7.8	19.9	14.1

sion from the accretion disk is reprocessed by dust. This increase in the L_{IR}/L_X ratio may therefore be due to larger AGN dust covering factors at higher redshifts; there is tentative evidence that this is indeed the case from measurements of the obscured to unobscured ratios of AGNs in deep X-ray surveys (e.g. La Franca et al. 2005; Hasinger 2008). Results presented in Hasinger (2008) predict a factor of ≈2 increase in the ratio of obscured-to-unobscured AGNs between $z = 0$ and $z = 1 - 2$, significantly lower than what we measure here. However, this is based on a sample of AGNs covering a broader range of L_X than focused on here and there is evidence that any increase in the dust covering fraction will be weaker in more X-ray luminous AGNs (e.g. Ueda et al. 2003; Akylas et al. 2006; Treister et al. 2008; and supported by the reduced L_{IR}/L_X ratios of the $L_X = 10^{43-44}$ erg s^{-1} AGNs reported here). Therefore, on the basis of the X-ray survey results, it is plausible that at least some of the increase in L_{IR}/L_X ratio is due to a larger dust covering factor at $z \approx 1 - 2$ than seen at lower redshifts. An increase in dust-covering factor with redshift is predicted by a number of theoretical models, which suggest that AGNs undergo early growth during a hidden phase before expelling their obscuring gas and dust, revealing a luminous, unobscured quasar (Silk & Rees 1998; Springel et al. 2005; Hopkins et al. 2006).

More direct constraints on the origin of the increase in the L_{IR}/L_X ratio will be placed using the *Herschel Space Observatory* (see §4.3) and *Spitzer*-IRS, for the fraction of X-ray AGNs that have *Spitzer*-IRS data (J. R. Mullaney, in preparation).

4.2 What is the contribution of AGNs to the cosmic IR background?

We can use the results of our stacking analysis to place constraints on the AGN contribution to the 70 μm background. If we stack all of the 251 X-ray AGNs, irrespective of whether they are individually detected at 70 μm we obtain an average 70 μm flux density of 1040±80 μJy, and therefore an integrated 70 μm flux density of 260±20 mJy, over the 391.3 arcmin^2 of the CDF-S field. On the basis of the analysis of the IR background in both GOODS fields and the Lockman Hole (e.g., Dole et al. 2006), this corresponds to ≳5% of the average resolved 70 μm background. This constraint is a lower limit since (1) the X-ray observations will not have identified the most heavily obscured luminous AGNs in this field, (2) the 70 μm field is too small to include X-ray bright AGNs, and (3) the X-ray observations are not sensitive to the lowest-luminosity AGNs.

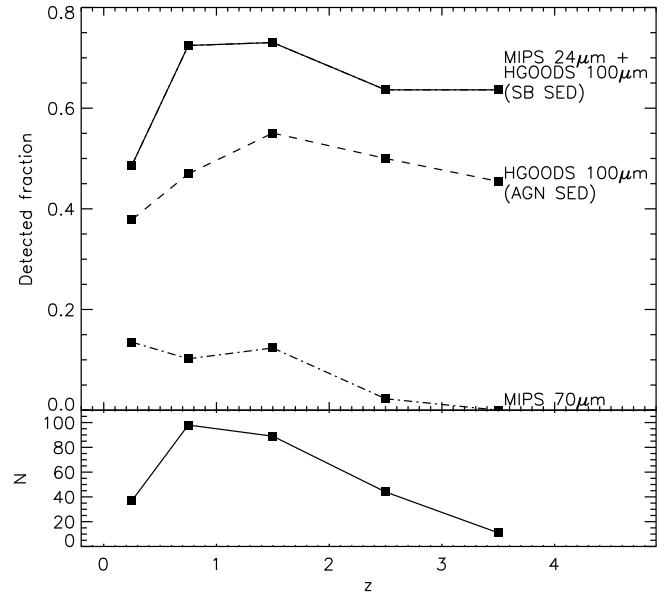On the basis of Tozzi et al. (2006), we would predict ≈80%

Figure 7. *Top:* Predicted fractions of CDF-S X-ray AGNs detected in the upcoming HGOODS deep infrared survey to be undertaken by the *Herschel Space Observatory*. The expected observed 100 μm flux densities are calculated by extrapolating the *Spitzer*-MIPS 24 μm flux densities along the Average SB-dominated and Average AGN-dominated SEDs, derived from the BAT/IRS sample of AGNs. If all the X-ray AGNs were to have SB-dominated IR SEDs, we would expect to detect *at least* as high a fraction at 100 μm as we currently detect at 24 μm. Also shown for comparison are the fractions of CDF-S AGNs detected by MIPS at 70 μm in each redshift bin *Bottom:* The number of CDF-S X-ray AGNs in each redshift bin.

of $L_X > 10^{41}$erg s^{-1}, $N_H < 10^{23}$ AGNs in the CDF-S (i.e., to $z \approx 5$) to be X-ray undetected. If we assume that they have the same IR SED as the X-ray detected AGNs then they increase our estimate of the resolved 70 μm background by a factor of five to ≳25%; from a study of nearby sources, Lutz et al. (2004) finds that the IR emission of AGNs is not significantly depressed in the most heavily obscured sources (we confirm that this is also the case for the BAT/IRS sample). Since X-ray surveys are insensitive to the most heavily obscured AGNs (i.e., Compton-thick sources with $N_H > 10^{24}$ cm^{-2}), the overall contribution to the 70 μm background could potentially double to ≳ 10% (e.g., Daddi et al. 2007; Alexander et al. 2008).

To estimate the contribution to the 70 μm background from bright AGNs that are too rare to lie in the small CDF-S field
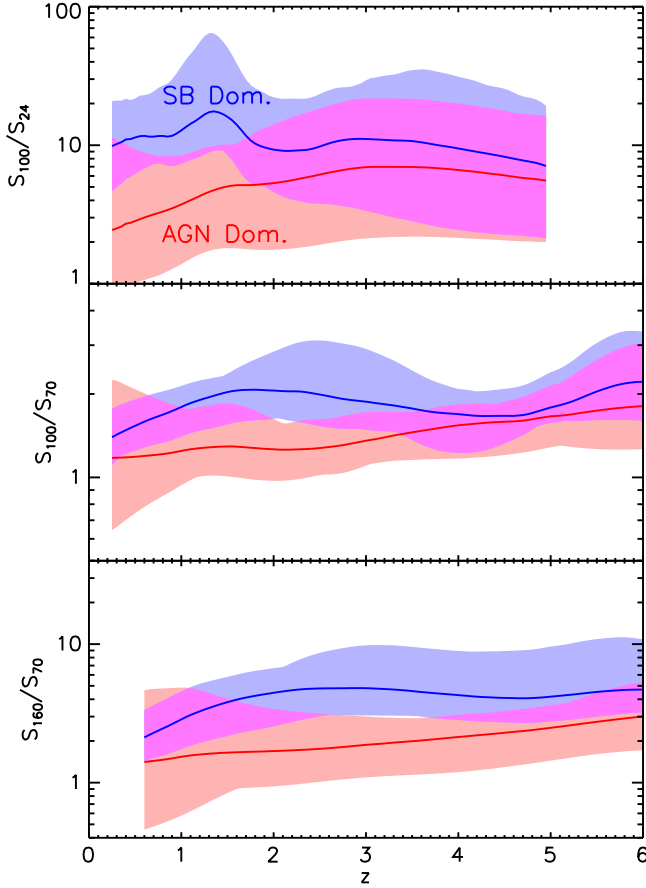
Figure 8. AGN/SB diagnostic powers of the PACS filters on board *Herschel Space Observatory*. The shaded regions indicate the range of expected flux ratios of the AGNs in the BAT/IRS sample at the redshifts shown. Solid lines indicate the expected flux ratios of the BAT/IRS Average AGN and Average SB.

would require the same analyses as performed here to be made on a shallower survey that covers a larger area of the sky. As it stands, the most accurate 70 μm analysis in a larger field is that of Papovich et al. (2007) of the E-CDFS. They find that bright AGNs (i.e., $L_X > 10^{44}$ erg s^{-1}) contribute only 7×10^{-4} MJy sr^{-1} to the IR background at 70 μm, corresponding to an insignificant fraction ($\ll 1\%$) of the total IR background at this wavelength. However, the E-CDFS field is not a great deal larger than the CDF-S field and a full study of the contribution of X-ray bright AGNs to the IR background will require the analysis of the much larger COSMOS[9] and/or Bootes[10] fields at 70 μm.

4.3 What advances may we expect for deep surveys with *Herschel*?

Our study of the FIR properties of X-ray detected AGNs allows us to place constraints on the properties of AGNs detected in deep *Herschel* fields at > 70 μm. We anticipate that the improved sensitivity of the *Herschel*-PACS instrument over *Spitzer*-MIPS will result in a significant increase in the fractions of X-ray AGNs that will be detected at FIR wavelengths, which will provide more direct

insight into the processes driving the increase in L_{IR} at $z = 1 - 2$. Depending on the assumed SED we predict that approximately 45-60%, 50-70%, 50-65% and 45-65% of the CDF-S X-ray sources at $z < 1$, $z = 1 - 2, 2 - 3$ and $3 - 4$, respectively, will be detected at 100 μm in the proposed ultradeep HGOODS survey (limiting flux = 0.6 mJy; see Fig. 7). These estimated detection levels are calculated by extrapolating the 24 μm flux densities along the Average SB-dominated and Average AGN-dominated SEDs (derived from the BAT/IRS sample).

In Fig. 8 we present the results of passing the IR spectra of the BAT/IRS sample through the various PACS filter response curves. Our analysis shows that, although the S_{100}/S_{24} flux ratio will not push our constraints on the relative contributions from AGN activity and star formation to higher redshifts (due to the influence of the MIR spectral features that shift into the observed 24 μm band at high redshifts), the S_{100}/S_{70} and S_{160}/S_{70} flux ratios will "take over" and provide this information out to a redshift of ~ 5 (i.e., the redshift of the most distant AGNs currently detected in the deepest X-ray surveys). Deep, infrared observations undertaken by *Herschel* will therefore provide a method of identifying a significant proportion of the long sought after population of Compton-thick AGNs out to $z \approx 6$.

5 SUMMARY

We have investigated the MIR and FIR properties of X-ray detected AGNs and SBs in the CDF-S using deep 24 μm and 70 μm observations undertaken by the *Spitzer Space Telescope* as part of the GOODS and FIDEL legacy surveys. Out of the 266 X-ray AGNs/SBs, 30 ($\approx 11\%$) and 172 ($\approx 65\%$) have counterparts at 70 μm and 24 μm respectively, with a bias towards the detection of SBs and BLAGNs at 70 μm. As the majority of CDF-S X-ray AGNs are undetected at 70 μm we rely on stacking analysis to measure their average MIR and FIR properties. We compare the IR properties of the CDF-S AGNs/SBs with those of a sample of local AGNs that have X-ray properties (i.e., L_X and N_H) covering the same range as the CDF-S AGNs (i.e., the BAT/IRS sample). In the following points we summarise the main conclusions of this study:

(i) We find strong evidence at both 24 μm and 70 μm that the average infrared luminosity of $L_X = 10^{42-43}$ erg s^{-1} AGNs at $z = 1 - 2$ is significantly higher than those at $z = 0.5 - 1$ and $z \approx 0$ (i.e., by a factor of ≈ 5 and ≈ 20, respectively). This difference corresponds to a factor of $4.7^{+10.2}_{-2.0}$ and $12.7^{+7.1}_{-2.6}$ increase in L_{IR}/L_X, respectively. This large increase in L_{IR} is not, however, seen for AGNs with higher X-ray luminosities (i.e., $L_X = 10^{43-44}$ erg s^{-1}). We therefore argue that deep IR observations can be used as a reliable method to identify intrinsically bright (i.e., $L_X = 10^{43-44}$ erg s^{-1}) Compton-thick AGNs, but urge caution when using this ratio to locate less luminous obscured AGNs (i.e., $L_X \lesssim 10^{43}$ erg s^{-1}), unless other indicators of AGN activity are present.

(ii) Due to the low numbers of AGNs detected at 70 μm we are unable to establish what process is driving this increase in the average L_{IR}; however, both increased star-formation and/or increased AGN dust covering factors are likely candidates. If the former, then the $z = 1 - 2$ epoch may represent a period of rapid growth of the bulge to black hole mass ratio. However, there is tentative evidence from X-ray observations that the dust covering fraction is, indeed, higher at large redshifts. We predict that forthcoming deep surveys to be carried out by the *Herschel Space Observatory* will enable us

to resolve what process is driving the increase in L_{IR}. See sections 3.2.2, 3.3, 4.1.

(iii) On average, more X-ray luminous CDF-S AGNs have lower S_{70}/S_{24} flux ratios. Based on the infrared properties of a sample of local AGNs with similar X-ray properties (i.e., L_X and N_H), we conclude that more X-ray luminous CDF-S AGNs have IR SEDs that are more AGN-dominated (rather than SB dominated). See section 3.2.1.

(iv) Despite measuring a large increase in L_{IR} among $z = 1 - 2$ AGNs (see point (i) above), we find that the X-ray detected AGNs in the CDF-S contribute only $\approx 5\%$ of the 70 μm background. However, if we extrapolate this fraction to take into account those $\approx 80\%$ of AGNs that are undetected in X-rays, we estimate that $\approx 25\%$ of the 70 μm background is attributable to AGNs. See section 4.2.

(v) We anticipate that the undertaking of deep, FIR surveys by the *Herschel Space Observatory* will allow us to detect between 40% and 75% of the X-ray detected AGNs in the 1 Ms CDF-S, depending on whether the infrared SEDs are predominantly AGN or SB-dominated, respectively. Furthermore, the FIR diagnostics used in our analysis can be directly applied to the PACS filters on board *Herschel* to enable us to discriminate between AGNs with SB-dominated or AGN-dominated infrared SEDs. See section 4.3.

REFERENCES

Akylas A., Georgantopoulos I., Georgakakis A., Kitsionas S., Hatziminaoglou E., 2006, A&A, 459, 693

Alexander D. M., Bauer F. E., Brandt W. N., Schneider D. P., Hornschemeier A. E., Vignali C., Barger A. J., Broos P. S., Cowie L. L., Garmire G. P., Townsley L. K., Bautz M. W., Chartas G., Sargent W. L. W., 2003, AJ, 126, 539

Alexander D. M., Bauer F. E., Chapman S. C., Smail I., Blain A. W., Brandt W. N., Ivison R. J., 2005, ApJ, 632, 736

Alexander D. M., Brandt W. N., Hornschemeier A. E., Garmire G. P., Schneider D. P., Bauer F. E., Griffiths R. E., 2001, AJ, 122, 2156

Alexander D. M., Chary R.-R., Pope A., Bauer F. E., Brandt W. N., Daddi E., Dickinson M., Elbaz D., Reddy N. A., 2008, ApJ, 687, 835

Antonucci R., 1993, ARA&A, 31, 473

Antonucci R. R. J., Miller J. S., 1985, ApJ, 297, 621

Barger A. J., Cowie L. L., Capak P., Alexander D. M., Bauer F. E., Fernandez E., Brandt W. N., Garmire G. P., Hornschemeier A. E., 2003, AJ, 126, 632

Bassani L., Dadina M., Maiolino R., Salvati M., Risaliti G., della Ceca R., Matt G., Zamorani G., 1999, ApJS, 121, 473

Bauer F. E., Alexander D. M., Brandt W. N., Schneider D. P., Treister E., Hornschemeier A. E., Garmire G. P., 2004, AJ, 128, 2048

Benson A. J., Bower R. G., Frenk C. S., Lacey C. G., Baugh C. M., Cole S., 2003, ApJ, 599, 38

Booth C. M., Schaye J., 2009, ArXiv e-prints, 0904.2572

Bower R. G., Benson A. J., Malbon R., Helly J. C., Frenk C. S., Baugh C. M., Cole S., Lacey C. G., 2006, MNRAS, 370, 645

Brandl B. R., Bernard-Salas J., Spoon H. W. W., Devost D., Sloan G. C., Guilles S., Wu Y., Houck J. R., Weedman D. W., Armus L., Appleton P. N., Soifer B. T., Charmandaris V., Hao L., Higdon J. A. M. S. J., Herter T. L., 2006, ApJ, 653, 1129

Brandt W. N., Hasinger G., 2005, ARA&A, 43, 827

Daddi E., Alexander D. M., Dickinson M., Gilli R., Renzini A., Elbaz D., Cimatti A., Chary R., Frayer D., Bauer F. E., Brandt W. N., Giavalisco M., Grogin N. A., Huynh M., Kurk J., Mignoli M., Morrison G., Pope A., Ravindranath S., 2007, ApJ, 670, 173

Dole H., Lagache G., Puget J.-L., Caputi K. I., Fernández-Conde N., Le Floc'h E., Papovich C., Pérez-González P. G., Rieke G. H., Blaylock M., 2006, A&A, 451, 417

Donley J. L., Rieke G. H., Pérez-González P. G., Rigby J. R., Alonso-Herrero A., 2007, ApJ, 660, 167

Downes A. J. B., Peacock J. A., Savage A., Carrie D. R., 1986, MNRAS, 218, 31

Dwelly T., Page M. J., 2006, MNRAS, 372, 1755

Elvis M., Wilkes B. J., McDowell J. C., Green R. F., Bechtold J., Willner S. P., Oey M. S., Polomski E., Cutri R., 1994, ApJS, 95, 1

Fiore F., Grazian A., Santini P., Puccetti S., Brusa M., Feruglio C., Fontana A., Giallongo E., Comastri A., Gruppioni C., Pozzi F., Zamorani G., Vignali C., 2008, ApJ, 672, 94

Frayer D. T., Huynh M. T., Chary R., Dickinson M., Elbaz D., Fadda D., Surace J. A., Teplitz H. I., Yan L., Mobasher B., 2006, ApJL, 647, L9

Gebhardt K., Bender R., Bower G., Dressler A., Faber S. M., Filippenko A. V., Green R., Grillmair C., Ho L. C., Kormendy J., Lauer T. R., Magorrian J., Pinkney J., Richstone D., Tremaine S., 2000, ApJL, 539, L13

Genzel R., Lutz D., Sturm E., Egami E., Kunze D., Moorwood A. F. M., Rigopoulou D., Spoon H. W. W., Sternberg A., Tacconi-Garman L. E., Tacconi L., Thatte N., 1998, ApJ, 498, 579

Georgantopoulos I., Georgakakis A., Rowan-Robinson M., Rovilos E., 2008, A&A, 484, 671

Giacconi R., Zirm A., Wang J., Rosati P., Nonino M., Tozzi P., Gilli R., Mainieri V., Hasinger G., Kewley L., Bergeron J., Borgani S., Gilmozzi R., Grogin N., Koekemoer A., Schreier E., Zheng W., Norman C., 2002, ApJS, 139, 369

Granato G. L., De Zotti G., Silva L., Bressan A., Danese L., 2004, ApJ, 600, 580

Guainazzi M., Matt G., Perola G. C., 2005, A&A, 444, 119

Hasinger G., 2008, A&A, 490, 905

Hopkins P. F., Hernquist L., Cox T. J., Di Matteo T., Robertson B., Springel V., 2006, ApJS, 163, 1

Horst H., Gandhi P., Smette A., Duschl W. J., 2008, A&A, 479, 389

Huynh M. T., Pope A., Frayer D. T., Scott D., 2007, ApJ, 659, 305

Kauffmann G., Haehnelt M., 2000, MNRAS, 311, 576

Kennicutt Jr. R. C., 1998, ARA&A, 36, 189

Krabbe A., Böker T., Maiolino R., 2001, ApJ, 557, 626

Krolik J. H., Begelman M. C., 1988, ApJ, 329, 702

La Franca F., Fiore F., Comastri A., Perola G. C., Sacchi N., Brusa M., Cocchia F., Feruglio C., Matt G., Vignali C., Carangelo N., Ciliegi P., Lamastra A., Maiolino R., Mignoli M., Molendi S., Puccetti S., 2005, ApJ, 635, 864

Lehmer et al. B. D., 2005, ApJS, 161, 21

Luo et al. B., 2008, ApJS, 179, 19

Lutz D., Maiolino R., Spoon H. W. W., Moorwood A. F. M., 2004, A&A, 418, 465

Magnelli B., Elbaz D., Chary R. R., Dickinson M., Le Borgne D., Frayer D. T., Willmer C. N. A., 2009, ArXiv e-prints

Magorrian J., Tremaine S., Richstone D., Bender R., Bower G., Dressler A., Faber S. M., Gebhardt K., Green R., Grillmair C., Kormendy J., Lauer T., 1998, AJ, 115, 2285

Mainieri V., Bergeron J., Hasinger G., Lehmann I., Rosati P., Schmidt M., Szokoly G., Della Ceca R., 2002, A&A, 393, 425

Mainieri V., Rosati P., Tozzi P., Bergeron J., Gilli R., Hasinger G., Nonino M., Lehmann I., Alexander D. M., Idzi R., Koekemoer A. M., Norman C., Szokoly G., Zheng W., 2005, A&A, 437, 805

Maiolino R., Shemmer O., Imanishi M., Netzer H., Oliva E., Lutz D., Sturm E., 2007, A&A, 468, 979

Malizia A., Bassani L., Stephen J. B., Di Cocco G., Fiore F., Dean A. J., 2003, ApJL, 589, L17

Marconi A., Hunt L. K., 2003, ApJL, 589, L21

McLure R. J., Dunlop J. S., 2002, MNRAS, 331, 795

Menéndez-Delmestre K., Blain A. W., Alexander D. M., Smail I., Armus L., Chapman S. C., Frayer D. T., Ivison R. J., Teplitz H. I., 2007, ApJL, 655, L65

Menéndez-Delmestre K., Blain A. W., Smail I., M. Alexander D., Chapman S. C., Armus L., Frayer D., Ivison R. J., Teplitz H., 2009, ApJ, 699, 667

Mushotzky R. F., Done C., Pounds K. A., 1993, ARA&A, 31, 717

Papovich C., Rudnick G., Le Floc'h E., van Dokkum P. G., Rieke G. H., Taylor E. N., Armus L., Gawiser E., Huang J., Marcillac D., Franx M., 2007, ApJ, 668, 45

Pope A., Chary R.-R., Alexander D. M., Armus L., Dickinson M., Elbaz D., Frayer D., Scott D., Teplitz H., 2008, ApJ, 675, 1171

Pope A., Scott D., Dickinson M., Chary R.-R., Morrison G., Borys C., Sajina A., Alexander D. M., Daddi E., Frayer D., MacDonald E., Stern D., 2006, MNRAS, 370, 1185

Richards G. T., Lacy M., Storrie-Lombardi L. J., Hall P. B., Gallagher S. C., Hines D. C., Fan X., Papovich C., Vanden Berk D. E., Trammell G. B., Schneider D. P., Vestergaard M., York D. G., Jester S., Anderson S. F., Budavári T., Szalay A. S., 2006, ApJS, 166, 470

Sanders D. B., Mirabel I. F., 1996, ARA&A, 34, 749

Silk J., Rees M. J., 1998, A&A, 331, L1

Springel V., Di Matteo T., Hernquist L., 2005, MNRAS, 361, 776

Stern D., Eisenhardt P., Gorjian V., Kochanek C. S., Caldwell N., Eisenstein D., Brodwin M., Brown M. J. I., Cool R., Dey A., Green P., Jannuzi B. T., Murray S. S., Pahre M. A., Willner S. P., 2005, ApJ, 631, 163

Szokoly G. P., Bergeron J., Hasinger G., Lehmann I., Kewley L., Mainieri V., Nonino M., Rosati P., Giacconi R., Gilli R., Gilmozzi R., Norman C., Romaniello M., Schreier E., Tozzi P., Wang J. X., Zheng W., Zirm A., 2004, ApJS, 155, 271

Tajer et al. M., 2007, A&A, 467, 73

Tozzi P., Gilli R., Mainieri V., Norman C., Risaliti G., Rosati P., Bergeron J., Borgani S., Giacconi R., Hasinger G., Nonino M.,

Streblyanska A., Szokoly G., Wang J. X., Zheng W., 2006, A&A, 451, 457

Treister E., Krolik J. H., Dullemond C., 2008, ApJ, 679, 140

Tremaine S., Gebhardt K., Bender R., Bower G., Dressler A., Faber S. M., Filippenko A. V., Green R., Grillmair C., Ho L. C., Kormendy J., Lauer T. R., Magorrian J., Pinkney J., Richstone D., 2002, ApJ, 574, 740

Tueller J., Mushotzky R. F., Barthelmy S., Cannizzo J. K., Gehrels N., Markwardt C. B., Skinner G. K., Winter L. M., 2008, ApJ, 681, 113

Ueda Y., Akiyama M., Ohta K., Miyaji T., 2003, ApJ, 598, 886

Winter L. M., Mushotzky R. F., Reynolds C. S., Tueller J., 2009, ApJ, 690, 1322

This paper has been typeset from a T$_{\rm E}$X/ L$^{\rm A}$T$_{\rm E}$X file prepared by the author.

APPENDIX A: THE *Swift*-BAT COMPARISON SAMPLE

To aid in the interpretation of the *Spitzer* MIPS data used to characterise the CDF-S X-ray sample, we selected a local sample of AGNs from the *Swift*-BAT survey with *Spitzer*-IRS low-resolution spectroscopy (5.2–38 μm). The *Spitzer*-IRS data allows us to accurately distinguish between AGNs with AGN-dominated and SB-dominated IR SEDs on the basis of the MIR spectral features in the *Swift*-BAT AGNs. The *Swift*-BAT survey provides the ideal local AGN comparison sample since the sensitivity of the BAT telescope to hard X-ray photons (14–195 keV) provides an almost absorption-independent selection of AGNs (to $N_{\rm H} \approx 10^{24}$ cm^{-2}). Indeed, the range of X-ray luminosities and absorbing column densities of the *Swift*-BAT AGNs are comparable to those of the CDF-S AGNs (see Tueller et al. 2008 and Winter et al. 2009); see §2.2.1.

Thirty-six of the 104 *Swift*-BAT AGNs with good-quality $L_{2-10\,keV}$ and $N_{\rm H}$ constraints from Winter et al. (2009) or Bassani et al. (1999) have both Short-Low (SL; 3.6" x 136.0"; $R \sim$ 60–127) and Long-Low (LL; 10.5" x 360"; $R \sim$ 57–126) *Spitzer*-IRS spectroscopy, providing full coverage at 5.2–38 μm. All 36 BAT/IRS AGNs were observed in staring-mode with two nod positions, which are required for background subtraction. Basic Calibrated Data (BCD) images were combined and cleaned as described in Goulding & Alexander (2009). Differing nod positions were subtracted from each other to produce background subtracted images before extracting the spectra using SPICE[11]. The objects were sufficiently bright and the observations were sufficiently short that there was no significant effect from latent charge build-up on the detector. Long-slit orders were clipped using the wavelength trim ranges given in Table 5.1 of the *Spitzer*-IRS Observers manual[12]. The continuum of each source in every order was fitted using a first or second-order polynomial. The spectra were then matched to give a single continuous spectrum for each source. Flux calibration was carried out using the latest available Spitzer-IRS calibration files (version 17.2) and is largely consistent with archival *IRAS* 25 μm flux densities (to within a factor of 2.5 in ≈97% of cases). The BAT/IRS AGNs have absorption corrected 2-10 keV luminosities spanning 4.3×10^{41} erg s^{-1} to 1.9×10^{44} erg s^{-1} and absorbing column densities in the range 2.5×10^{20} cm^{-2} to 2.2×10^{24} cm^{-2}

---

[11] URL: http://ssc.spitzer.caltech.edu/postbcd/spice.html
[12] The *Spitzer*-IRS Observers Manual is available at http://ssc.spitzer.caltech.edu/irs/dh/
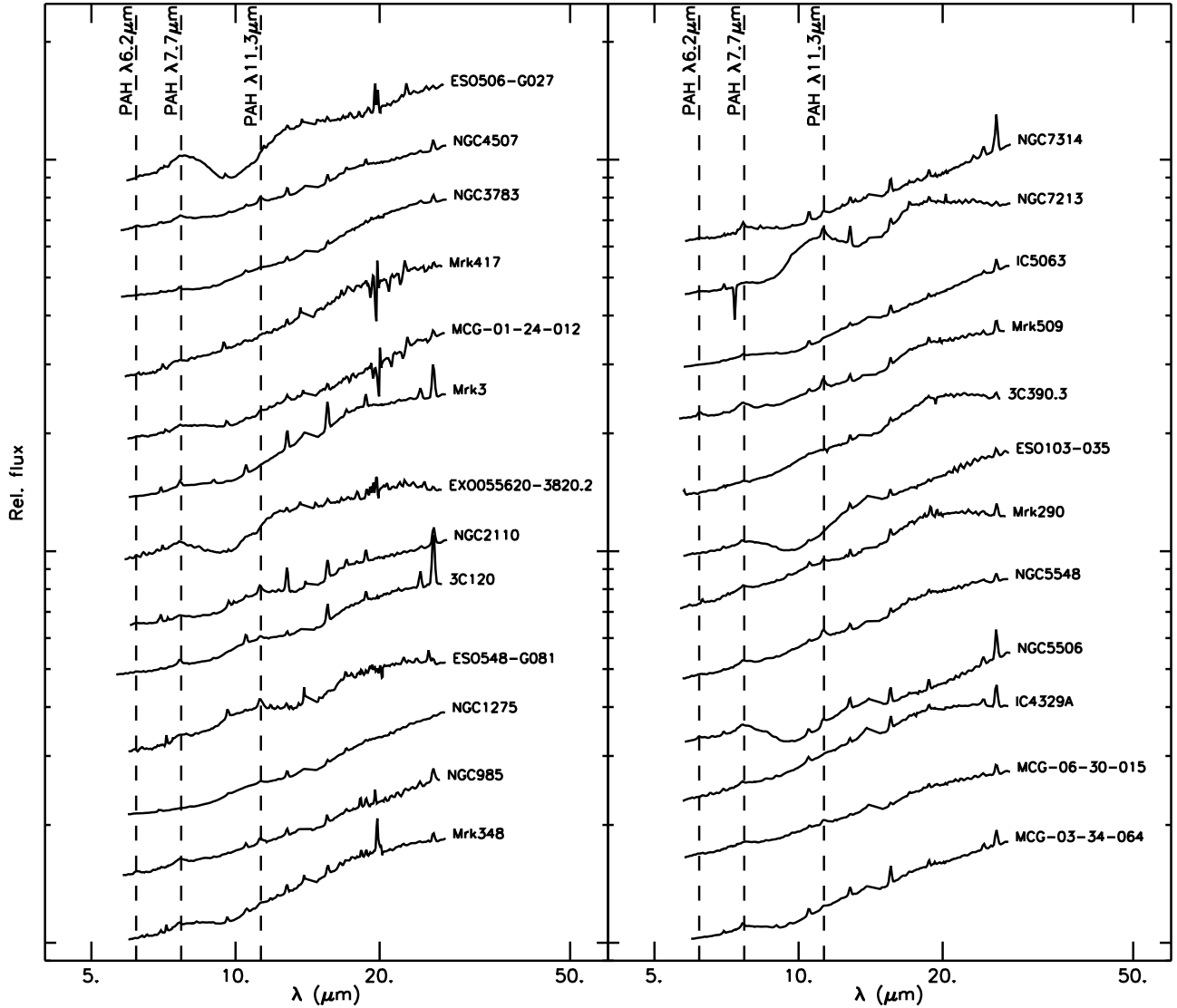
Figure A1. IRS spectra of the 25 BAT/IRS AGNs that we classify as having AGN-dominated IR SEDs on the basis of the lack of a prominent PAH feature at 6.2 μm. Also indicated are the PAH features at 7.7 μm and 11.4 μm although these were not used to distinguish between AGN and SB dominated systems.

(i.e., roughly the same as those CDF-S X-ray AGN/SBs with L_X and N_H measurements published in Tozzi et al. 2006).

To determine whether the S_{70}/S_{24} flux ratio can distinguish between SB and AGN dominated systems, we classified the BAT/IRS sample into those objects with a) a prominent PAH feature at 6.2 μm, which we assume is a good indicator of a strong starburst component (SB-dominated; e.g., Genzel et al. 1998; 11 objects), and b) a power-law MIR to FIR continuum with no sign of any PAH feature at 6.2 μm, which we assume indicates an AGN-dominated object (25 objects). The 6.2 μm PAH feature is preferred over other lines as it lies in a region of the IR spectrum that is largely free of other strong spectral features, in particular the silicate absorption/emission band at 9.7 μm. We show the *Spitzer*-IRS spectra of the BAT/IRS sample in Fig. A1 (AGN-dominated systems) and Fig. A2 (SB-dominated systems).

To calculate the expected S_{70}/S_{24} flux ratio tracks each of for the 36 BAT/IRS AGNs as a function of redshift, we shift each spectrum by a factor of $1+z$ in wavelength (where z is increased from 0.25 to 2.5 in steps of 0.025) and pass the resulting spec-

trum through the MIPS 24 μm and 70 μm filters. To determine the observed 70 μm fluxes at $z < 0.75$ requires knowledge of the IR SED beyond the wavelength coverage of the *Spitzer*-IRS spectra (i.e., > 38 μm). To provide this longer wavelength coverage, we extrapolated the longest wavelength bin of the IRS spectra to the 60 μm and 100 μm flux densities from the *IRAS* Point Source and Faint Source Catalogues[13]. Thirty-two of the 36 AGNs with IRS data have well constrained *IRAS* 60 μm and 100 μm fluxes. The remaining 4 (all classed as AGN dominated) have *IRAS* 60 μm or 100 μm flux densities that are flagged as upper limits in the *IRAS* catalogues. However, including these faint sources in our average AGN SED by assuming the upper limits as detections has no effect on any of our results. In Fig. A3, we show the S_{70}/S_{24} flux ratios derived from the BAT/IRS sample as a function of redshift. There is a clear separation between AGN and SB dominated systems at $z \lesssim 1.5$, showing that the S_{70}/S_{24} flux ratio can be used as an effi-
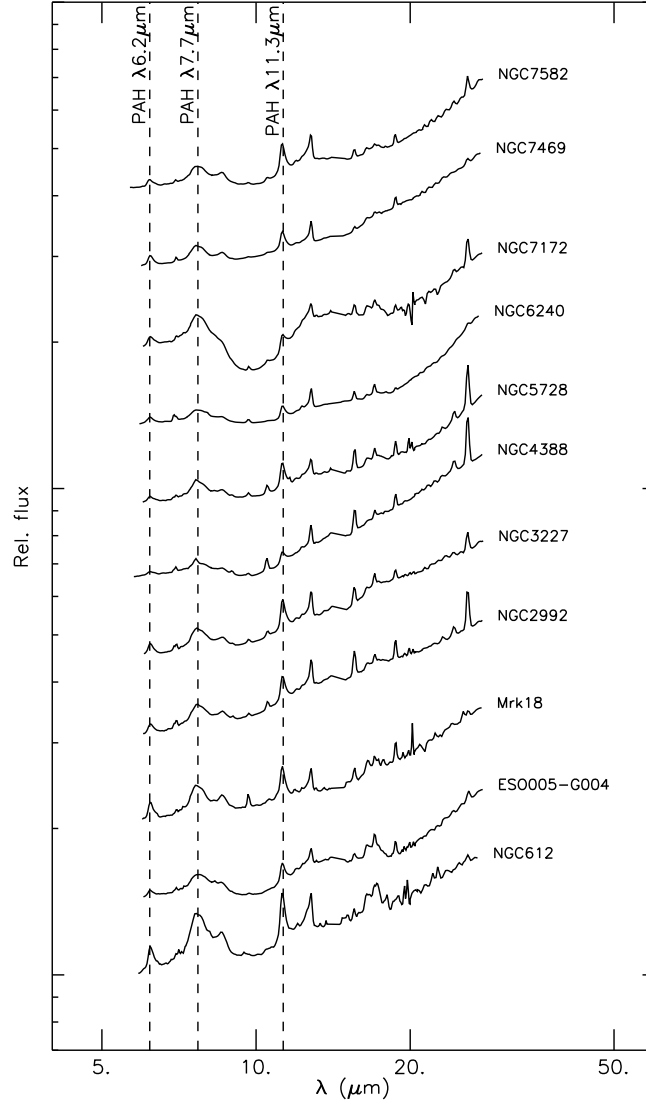
Figure A2. IRS spectra of the 11 BAT/IRS AGNs that we classify as having SB-dominated IR SEDs on the basis of the presence of a prominent PAH feature at 6.2 μm. Also indicated are the PAH features at 7.7 μm and 11.4 μm although these were not used to distinguish between AGN and SB dominated systems.

cient method to determine whether AGN or star-formation activity dominates the IR emission of X-ray detected AGNs.

Calculating L_{IR} for high redshift sources using the 24 μm flux density alone is susceptible to systematic errors caused by spectral features that are redshifted into this waveband at $z > 0.7$. We can use the BAT/IRS sample to establish the uncertainties in deriving L_{IR} from either 70 μm or 24 μm data. In the lower panels of Fig. A3 we show the expected observed frame 70 μm and 24 μm fluxes for the BAT/IRS sample, if observed at z=0.25-2.5 and normalised to $L_{IR} = 10^{12}$ L$_\odot$ (the normalisation factor, 10^{12} L$_\odot$/L_{IR}, is derived by calculating L_{IR} from the *IRAS* flux densities using the equations presented in Table 1 of Sanders & Mirabel 1996). Depending on the shape of the IR SED, sources of the same L_{IR} can differ in their observed 24 μm flux density by up to a factor of $\approx$12 at $z > 1$, compared to factor of only $\approx$3 at 70 μm. This range of 70 μm flux density is almost independent of redshift out to $z = 2.5$, indicating that S_{70} is up 4 times more accurate for determining L_{IR} when no information on the SED shape is available.
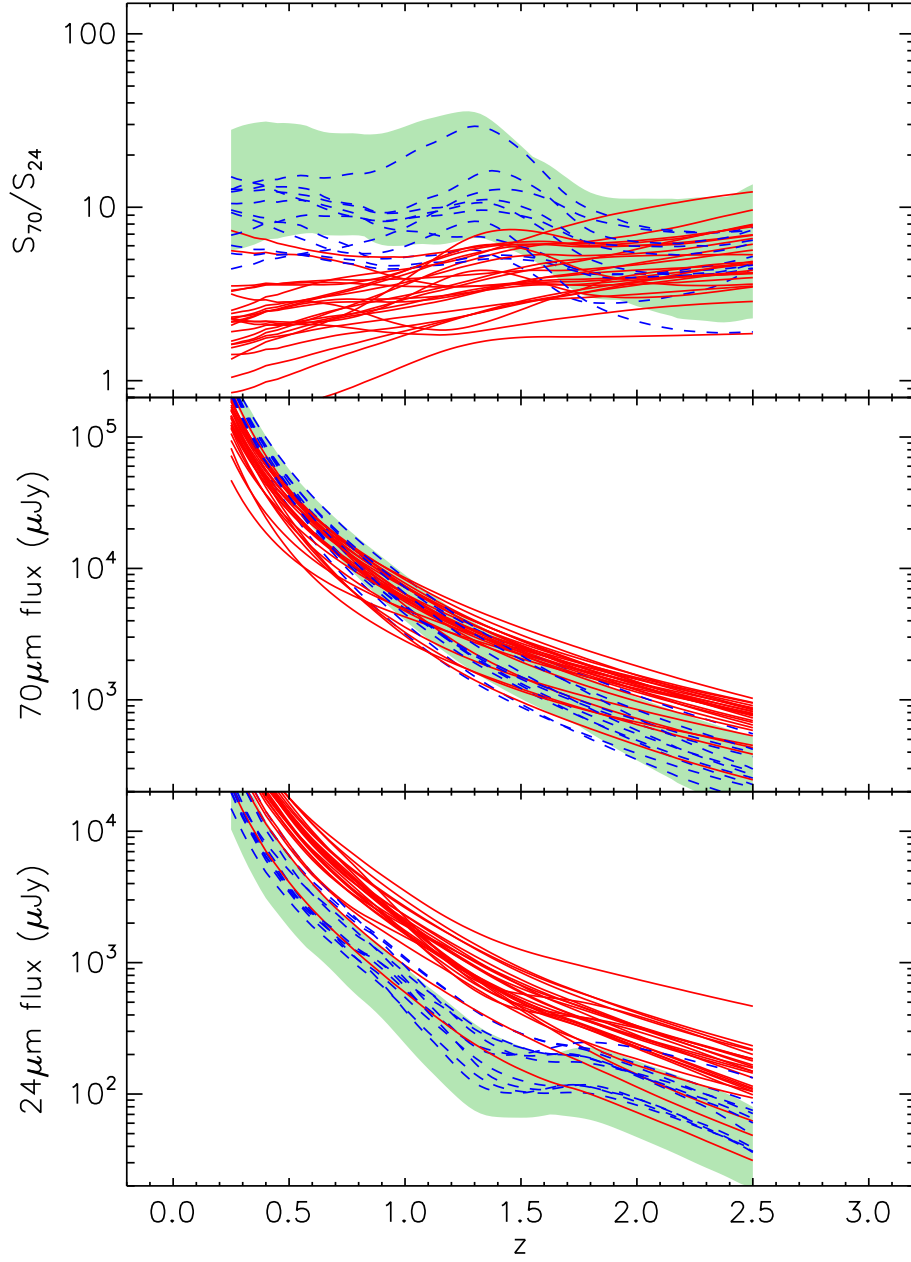
Figure A3. *Top:* The expected S_{70}/S_{24} flux ratio of the AGNs in the BAT/IRS AGNs over the redshift range $z = 0.25 - 2.5$. *Middle:* The expected observed 70 μm flux densities of the BAT/IRS AGNs over the redshift range $z = 0.25 - 2.5$, each normalised to $L_{IR} = 10^{12}$ L$_\odot$. *Bottom:* The expected observed 24 μm flux densities of the BAT/IRS AGNs over the redshift range $z = 0.25 - 2.5$, again normalised to $L_{IR} = 10^{12}$ L$_\odot$. We show the ratios and flux densities as expected if the AGNs were to be observed at $z = 0.25 - 2.5$. Solid, red lines refer to AGN-dominated and dashed blue lines to SB-dominated AGNs. The green shaded areas indicate the range of ratios and flux densities spanned by the Brandl et al. (2006) starburst galaxies over the redshift range $z = 0.25 - 2.5$.